Title

Determination of the nanoparticle- and cell-specific toxicological mechanisms in 3D liver spheroids using scRNAseq analysis

Author

xia, tian

Publication Date

2022-10-14

Peer reviewed

Nano Today 47 (2022) 101652

Contents lists available at ScienceDirect

Nano Today

journal homepage: www.elsevier.com/locate/nanotoday

Determination of the nanoparticle- and cell-specific toxicological mechanisms in 3D liver spheroids using scRNAseq analysis

Jiulong Li [a,b,1], Graciel Diamante [d,1], In Sook Ahn [d], Darren Wijaya [d], Xiang Wang [a,b], Chong Hyun Chang [a,b], Sung-min Ha [d], Kavya Immadisetty [d], Huan Meng [a,b], André Nel [a,b,*], Xia Yang [c,d,**], Tian Xia [a,b,*]

[a] Center of Environmental Implications of Nanotechnology (UC CEIN), California Nanosystems Institute, University of California, Los Angeles, CA 90095, USA
[b] Division of NanoMedicine, Department of Medicine, California Nanosystems Institute, University of California, Los Angeles, CA 90095, USA
[c] Molecular Toxicology Interdepartmental Program, University of California, Los Angeles (UCLA), Los Angeles, CA 90095, USA
[d] Department of Integrative Biology and Physiology, University of California, Los Angeles (UCLA), Los Angeles, CA 90095, USA

ARTICLE INFO

Article history:
Received 24 May 2022
Received in revised form 14 September 2022
Accepted 5 October 2022
Available online xxxx

Keywords:
Nanosafety
ScRNAseq
3D liver spheroids
Nanomaterials
Toxicological mechanisms

ABSTRACT

Engineered nanomaterials (ENMs) are commonly used in consumer products, allowing exposure to target organs such as the lung, liver, and skin that could lead to adverse health effects in humans. To better reflect on toxicological effects in liver cells, it is important to consider the contribution of hepatocyte morphology, function, and intercellular interactions in a dynamic 3D microenvironment. Herein, we used a 3D liver spheroid model containing hepatocyte and Kupffer cells (KCs) to study the effects of three different material compositions, namely vanadium pentoxide (V_2O_5), titanium dioxide (TiO_2), or graphene oxide (GO). Additionally, we used single-cell RNA sequencing (scRNAseq) to determine the nanoparticle (NP) and cell-specific toxicological responses. A general finding was that hepatocytes exhibit more variation in gene expression and adaptation of signaling pathways than KCs. TNF-α production tied to the NF-κB pathway was a commonly affected pathway by all NPs while impacts on the metabolic function of hepatocytes were unique to V_2O_5. V_2O_5 NPs also showed the largest number of differentially expressed genes in both cell types, many of which are related to pro-inflammatory and apoptotic response pathways. There was also evidence of mitochondrial ROS generation and caspase-1 activation after GO and V_2O_5 treatment, in association with cytokine production. All considered, this study provides insight into the impact of nanoparticles on gene responses in key liver cell types, providing us with a scRNAseq platform that can be used for high-content screening of nanomaterial impact on the liver, for use in biosafety and biomedical applications.

Introduction

The widespread use of engineered nanomaterials (ENMs) in applications such as cosmetics, food packaging, water purification, insecticides, electronics, and a number of biomedical applications is likely to lead to human exposure by dermal contact, inhalation, ingestion, or intravenous injection [1–4]. This necessitates the assessment of potential adverse health effects, for which we need appropriate methods for safety assessment [5,6]. The lung is a major target organ for inhaled ENMs, while the liver is the primary target organ for therapeutic nanoparticles and ENMs that have gained access to circulation following dermal contact, inhalation, and ingestion [7–9]. Compared to the lung, the effects of ENMs on the liver are under-investigated disproportionate to the level of importance.

The liver is the largest solid organ in the body and capable of performing many vital functions. These include removing waste products and foreign substances from the bloodstream, producing albumin, cholesterol, and bile, regulating amino acids and blood clotting, storing vitamins and minerals, and processing and storing glucose [10–13]. The liver is comprised of a variety of different cell types, including hepatocytes as the parenchymal component,

* Correspondence to: Department of Medicine, Division of NanoMedicine, UCLA School of Medicine, 52-175 CHS, 10833 Le Conte Ave, Los Angeles, CA 90095-1680, USA.
** Correspondence to: Department of Integrative Biology and Physiology; Molecular Toxicology Interdepartmental Program, UCLA, 2000C TLSB, Los Angeles, CA 90095, USA.
E-mail addresses: anel@mednet.ucla.edu (A. Nel), xyang123@ucla.edu (X. Yang), txia@ucla.edu (T. Xia).
[1] These authors contributed equally.

https://doi.org/10.1016/j.nantod.2022.101652

making up 60–80% of all liver cells, as well as non-parenchymal cells contributing 20–40% of cells in the liver [12,14]. Hepatocytes play key roles in protein synthesis, metabolism, endocrine, secretory, and detoxification pathways [9,14]. Kupffer cells (KCs) are liver resident macrophages that make up to 20% of nonparenchymal cells in the liver and are a key component of the mononuclear phagocyte system. KCs play a key role in the phagocytosis of ENMs from the sinusoidal circulation, modulation of innate immune responses, and endotoxin removal, acting as the first line of defense against circulating particulates [15–17]. Altogether, the specialized functions, localization, and interactions among different liver cell types are critical in shaping hepatic function, including in response to foreign substances such as ENMs [10,11]. It is therefore not a surprise that nanoparticles' entrance from the portal vein and the hepatic artery can lead to the exposure and generation of adverse effects on liver cells [9,14,18]. However, while most studies have concentrated on gross changes in liver function and histology, there is a lack of mechanistic understanding of the impact of different ENMs compositions on individual liver cell types, including during intercellular interactions, which exert a strong influence on cell function as compared to the response of individually cultured cells.

Liver cell-type-specific ENM effects and the possibility of toxicity are typically studied using traditional two-dimensional (2D) cell culture models [19,20]. However, many studies have demonstrated that the culture and attachment of liver cells as a single layer on a culture dish surface do not accurately predict biological and toxicological responses to ENMs in the intact organ due to altered morphology and the lack of intercellular communication [21,22]. For instance, conventional 2D cultures have shown that ENMs are capable of inducing a tiered oxidative stress response, which includes protective, pro-inflammatory, and cytotoxic effects [5,6]. The protective effect is mediated by low-level oxidative stress-induced binding of the nuclear factor erythroid 2–related factor 2 to the antioxidant response element and a number of phase II antioxidant enzymes (*e.g.*, catalase and superoxide dismutase), yielding to the activation of mitogen-activated protein kinase and nuclear factor kappa B (NF-κB) pathways at intermediary levels of oxidative stress levels, which promote pro-inflammatory cytokine and chemokine production [5,19,20]. Moreover, high levels of oxidative stress are capable of perturbing the mitochondrial permeability transition pore (MPTP) and energy transduction, leading to cellular apoptosis or necrosis [18–20]. In contrast, few such studies have been executed under 3D culture conditions, which could change thresholds for the tiered oxidative stress outcomes.

It has now become possible to study the effects of ENMs in liver spheroids, comprised of single or a mixture of cell types (*e.g.*, hepatocytes and KCs), which preserve cell morphology and can be kept in culture for prolonged observation periods [23–25]. In addition, many spheroid studies have shown their superiority in maintaining cell shape and morphology, cell-cell interactions, and gene as well as protein expression profiles, mimicking the liver in its response to exposure to drugs or chemicals (Supplemental Table 1). We argued, therefore, that the use of spheroids would be more appropriate for studying ENMs' adverse effects, especially if the assessment can be combined with a high throughput platform.

Recent technological advancements in high-throughput single-cell omics methods such as single-cell RNA sequencing (scRNAseq) offer revolutionary opportunities to build a comprehensive and explanatory map of the molecular pathways induced by agents in an unbiased manner and at a single-cell resolution [26]. This has become a gold standard for defining cell states and phenotypes in recent years [27,28], and can provide information about the existence and behavior of various cell types in the same tissue or organ [29]. Furthermore, a population with the same cell type may appear to be genetically homogeneous in macrosystems, but scRNAseq can uncover cell-to-cell heterogeneity, reflecting cell populations that adapt quickly to changing conditions [30,31]. The use of scRNAseq technology in a 3D liver model can contribute to a greater understanding of the toxicological molecular mechanisms of ENMs in different types of liver cells.

In this study, we used scRNAseq to elucidate how different nanomaterials affect gene expression programs in different liver cell types. We chose to study vanadium pentoxide (V_2O_5), graphene oxide (GO), and titanium dioxide (TiO_2) as three representative nanomaterial categories that have yielded contrasting response outcomes under conventional culture conditions. V_2O_5 nanoparticles (NPs) are extensively used as a catalyst in industrial chemical processes, which can lead to occupational exposures in workers [32,33]. TiO_2 NPs are used as a pigment in paints, food additives, and sunscreens, with the potential to lead to oral, dermal, and occupational exposure in people [34,35]. GO nanosheets, a representative two-dimensional (2D) nanomaterial, are frequently used for tissue engineering, antimicrobial agents, drug carriers, and biosensors, with the ability to lead to human exposures *via* dermal, inhalation, ingestion, and intravenous routes [36]. Widespread use of these ENMs also increases the potential for adverse impacts on the liver, which can be reached *via* intravenous use or indirectly following absorption in the gastrointestinal tract or access *via* the lung (Supplemental Table 2). Moreover, we have shown that V_2O_5 and GO are capable of inducing cytotoxic effects on liver cells in 2D culture [37,38], and have used TiO_2 in numerous previous ENM toxicity studies as an insoluble, low-toxicity material. A hanging drop technique was used to construct 3D liver spheroids containing KCs and hepatocytes. Following the exposure to V_2O_5, GO, and TiO_2, scRNAseq was used for transcriptomic profiling of the constituent cell types to identify cell-specific gene responses as well as biomarkers and pathways that are affected by each ENM. We also use supporting immunostaining and enzyme-linked immunosorbent assays (ELISA) to confirm cellular responses and cytokine production, as predicted by scRNAseq profiling.

Methods

V_2O_5, TiO_2, and GO NPs were provided by Engineered Nanomaterials Resource and Coordination Core, part of the Nanomaterial Health Implications Research (NHIR) Consortium of the National Institute of Environmental Health Sciences (NIEHS). The transformed mouse Kupffer cell line, KUP5, was purchased from RIKEN Cell Bank (Japan). The mouse hepatocyte cell line, Hepa 1–6, was purchased from ATCC (Manassas, VA). Fetal bovine serum (FBS) was purchased from Gemini Bio-Products (West Sacramento, CA). Penicillin-streptomycin was purchased from Gibco (Waltham, MA). The ATPlite 1step Luminescence Assay kit was purchased from PerkinElmer Inc. (Waltham, MA). Hoechst 33 342 was purchased from Life Technologies (Grand Island, NY). The MitoSOX indicator was purchased from Invitrogen (Carlsbad, CA). FITC (90%) was purchased from ACROS Organics (Fair Lawn, NJ) and the FAM-FLICA Caspase-3/7 assay kit was purchased from ImmunoChemistry Technologies, LC (Bloomington, MN). The ELISA kits for mouse IL-1β and TNF-α were purchased from R&D Systems (Minneapolis, MN).

Characterization of nanomaterials

The size and morphology of GO, TiO_2, or V_2O_5 NPs were characterized in-house in the California NanoSystems Institute by transmission electron microscopy (TEM, JEOL 1200-EX transmission electron microscope) without further purification or modification. The hydrodynamic diameters, polydisperse index (PDI), and zeta potential of the NP suspensions were determined by a ZetaPALS instrument (Brookhaven Instrument, Holtsville, NY). Briefly, the stock NP solutions at a concentration of ≈ 1 mg/mL in DI water were prepared and sonicated for 1 min. These suspensions were

subsequently diluted to a final concentration of 50 μg/mL in DI water or cell culture media, followed by further sonication for 1 min.

Cell culture

The transformed hepatocyte cell line, Hepa 1–6, and Kupffer cell line, KUP5, were chosen for this study, based on similarities in their response to nanoparticles in primary and human cell lines (Supplemental Table 3), as well as stable phenotype, ease of culture, ready availability and low cost [19,22–26]. Moreover, the use of cell lines also avoids inter-donor variations in establishing proof-of-principle testing. Specifically, KUP5 cells were cultured in high-glucose Dulbecco's modified eagle medium (DMEM), supplemented with 10% FBS (Gemini Bio-Products, West Sacramento, CA), 250 μM 1-thioglycerol, 10 μg/mL bovine insulin, and 100 U/mL/100 μg/mL of penicillin-streptomycin (Gibco, Waltham, MA). Hepa 1–6 cells were cultured in a high-glucose DMEM medium supplemented with 10% FBS and 100 U/mL/100 μg/mL penicillin-streptomycin. All cells were cultured in a humidified environment of 95% O_2, 5% CO_2, and 37 °C.

3D liver spheroids

The 3D liver spheroids, containing hepatocytes (Hepa 1–6) and KCs (KUP5) at a 9:1 ratio (to mimic the *in vivo* cell ratio), were prepared by a hanging drop technique, using the 3D Biomatrix Hanging Drop Plate (3D Biomatrix, Ann Arbor, MI, USA). Briefly, 20 μL of cell suspension at ~100 cells/μL was pipetted from the upper surface of the plate, with the pipette tip inserted into the neck region, before the slow release of the cell suspension. Following the formation of the hanging droplets, ~2 mL of distilled water was added to the plate's water reservoir. The plates were subsequently incubated at 37 °C under a humidified atmosphere and 5% CO_2 in an incubator. To improve the formation of the 3D liver spheroids, 2–5 μL of fresh media was added to the culture every other day. The size and form of the spheroids were evaluated by light microscopy (Zeiss Axio Observer D1; Carl Zeiss AG, Jena, Germany).

Exposure of NPs to 3D liver spheroids

NP dispersions were freshly prepared by pre-incubating in a complete cell culture medium before cellular exposure. For cytotoxicity experiments, the 3D liver spheroids were incubated with particle dispersions over a wide concentration range (1.5625, 3.125, 6.25, 12.5, 25, 50, or 100 μg/mL) for 24 h, as previously reported [19,20,37,38]. Cell viability was accessed using the ATPlite 1-step assay (PerkinElmer Inc, Waltham, MA) to quantify cellular ATP content, according to the manufacturer's instructions. The luminescence intensity was read on a SpectraMax M5 microplate reader. Control cells, not subjected to ENMs exposure, were regarded as representing 100% cell viability, according to which the viability of the treated cells was adjusted. Fluorescence-labeled NPs were prepared as previously described by us and used to demonstrate the cellular association or uptake of NPs in 3D liver spheroids, using an ENM concentration of 25 μg/mL for 16 h [37,38].

Collection of single-cell suspensions

In order to limit the cell death rate to < 5% (as determined by the ATP assay) for scRNA sequencing, the mouse liver spheroids were exposed to the ENMs at 6.25 μg/mL for 6 h. The cultured 3D liver spheroids were collected in a 1.5 mL tube and washed three times with PBS to remove cell debris and ENMs by centrifugation (1400 rpm for 5 min). The harvested spheroids were dissociated using 5 mg/mL collagenase (Sigma-Aldrich Co. St. Louis, MO) for 2 h at 37 °C. The dissociated cells were washed and collected by centrifugation and resuspended in ~500–1000 μL of a 0.04% BSA/PBS solution. Subsequently, the cell suspension was filtered through a 40 μm (mini) strainer. Cells were centrifuged and resuspended in a 60 μL of 0.04% BSA/PBS, yielding cell concentrations of 300–1200 cells/μL. Each NP or control treatment was done in duplicate and each replicate was used for independent scRNAseq analysis.

scRNAseq data generation and preprocessing

Single-cell RNA-sequencing was conducted following the 10× 3′ single-cell RNA-seq V3.1 protocol (10x Genomics, Pleasanton, California, USA). The cDNA library concentration was determined using the Qubit Fluorometric Quantitation method (Thermofisher Scientific, Waltham, MA, USA), and quality was assessed using the Agilent TapeStation system (Agilent, Santa Clara, CA, USA). The libraries were sequenced on the Novaseq S1 2 × 50bp (Illumina, San Diego, CA, USA) in the UCLA Broad Stem Cell Research Center at ~25k reads/cell. Illumina sequencer's base call files (BCLs) were demultiplexed and fastq files were generated using the mkfastq function on the Cell Ranger software version 3.0.2 (10x Genomics, Pleasanton, California, USA). Single-cell sequencing reads were aligned to the mouse reference genome (mm10–3.0.0) and the gene-cell count matrices from each sample were processed using Seurat version 3.1 [https://github.com/satijalab/Seurat] [39]. Single cells were filtered based on a threshold of between 200 and 7000 genes, a maximum of 50,000 unique molecular identifiers (UMIs), less than 10% mitochondrial gene expression, and 50% ribosomal protein gene expression. Gene counts were normalized using the default NormalizeData function (log normalize method) in Seurat. Raw sequencing reads were submitted to Gene expression omnibus (GEO) under the accession number GSE201500.

Cell cluster identification, differential gene expression analysis, and pathway analysis

All 8 scRNAseq samples (2 replicates per ENM plus the non-treated control) were integrated using the canonical correlation analysis method in Seurat. Cells were projected onto two dimensions, using t-SNE based on the top 30 principal components of the gene expression profiles, and assigned into clusters using the Louvain clustering method. Marker genes used to identify hepatocytes and KCs were curated based on previous studies [40–42] and were used to determine cell identities according to scRNAseq data. Using the FindAllMarkers function in Seurat, positive gene markers were obtained for hepatocyte and KC spheroid-derived cells. Positive gene markers identified in the 3D spheroid hepatocyte and KCs were compared to the adult liver cell type markers from the Mouse cell atlas (MCA) [43,44]. The mouse Hepatocyte_combined markers are the collective markers identified from Hepatocyte_spp1 High, Hepatocyte_fabp1 High, Hepatocyte_mt High, Hepatocyte_alb High, and Hepatocyte_car3 High clusters. The positive gene markers identified in the 3D spheroid hepatocyte and KCs were also compared to human reference cell type markers derived from a human scRNA-Seq dataset, under the accession number GSE115469 [45]. The human Hepatocyte_combined markers are the collective markers identified from Hepatocyte_1 – Hepatocyte_6 clusters. The GeneOverlap package on R was used to evaluate the overlap of the marker genes. The statistical significance of marker overlap was determined using Fisher's exact test. After cell type identification, the Seurat FindMarkers function (non-parametric Wilcoxon rank-sum test) was used to compare gene expression between the control and ENM-treated cells. For each exposed cell type, genes with an adjusted *p*-value (based on Bonferroni correction) threshold < 0.05 and a log fold change (logFC) threshold > 0.1, were identified as differentially expressed genes (DEGs) compared to control cells. However, due to the limited DEGs identified in KCs, the unadjusted *p*-value < 0.05 was used as a threshold. Among the selected genes,

those displaying the same direction of increase or decrease in the two replicates were considered as significant DEGs for the particular ENM. For plotting purposes, the average logFC between the biological replicate was calculated and the adjusted *p*-values (hepatocytes) or the unadjusted *p*-values (KCs) of the DEGs from the two biological replicates were combined with the Benjamini-Hochberg method from the Metap package in R.

We also performed pathway enrichment analysis for the identified DEGs mentioned, using the KEGG, BioCarta, Reactome, and Hallmark pathway databases from MSigDB. Significant enrichment of pathways was based on a hypergeometric test followed by multiple testing corrections using the Stouffer method. Pathways that were considered significant had an FDR < 0.05.

Determination of mtROS generation

The 3D liver spheroids were exposed to 25 μg/mL of NPs for 16 h. Following PBS washing, spheroids were treated with 5 μm MitoSOX (Invitrogen, Carlsbad, CA) in HBSS at 37 °C for 30 min and then stained with 5 μg/mL Hoechst 33 342 (Life Technologies, Grand Island, NY) for 45 min. Imaging was performed in a Zeiss Axio Observer D1 fluorescent microscope, with quantification of cellular fluorescence intensity by a SpectraMax M5 microplate reader at excitation/emission wavelengths of 510/580 nm.

Determination of caspase-1 activation

The 3D liver spheroids were exposed to 25 μg/mL NPs and washed three times in PBS, before staining with FAM-FLICA Caspase-3/7 substrates (ImmunoChemistry Technologies, LC, Bloomington, MN) at 37 °C for 1 h. Cells were subsequently also stained with Hoechst 33 342 for 30 min and imaged under a fluorescent microscope. Quantification of cellular fluorescence intensity was obtained by a microplate reader, using excitation/emission wavelengths of 492/520 nm.

Determination of IL-1β, TNF-α, and TGF-β1 production

The 3D liver spheroids were primed by replacing the tissue culture medium with a fresh medium containing 1 μg/mL lipopolysaccharide (LPS) for 4 h, followed by the exposure to 25 μg/mL of each ENM suspension, supplemented with 0.1 μg/mL LPS for 24 h. The cellular supernatants were collected for IL-1β, TNF-α, and TGF-β1 quantification by ELISA, according to the manufacturer's instructions (R&D Systems, Minneapolis, MN).

AST release by the 3D liver spheroid after nanoparticle treatment

3D liver spheroids were exposed to 25 μg/mL of each ENM suspension. The supernatants were collected for AST quantification by the Mouse Aspartate Aminotransferase ELISA Kit from Novus Biologicals, LLC.

Results

ENM characterization

The physicochemical characterizations of V_2O_5, TiO_2, and GO nanomaterials are detailed in Fig. 1 and Table 1. As shown by TEM images in Fig. 1A, V_2O_5 NPs displayed irregular shapes with a size of 380.0 ± 223.1 nm. TiO_2 NPs showed spherical shapes with a size of 125.0 ± 45.7 nm, while GO was comprised of sheet-like structures with diameters of 589.8 ± 340.5 nm. Furthermore, the dispersibility of NPs in aqueous solutions was assessed by hydrodynamic size and zeta potential in DI water and cell culture medium, respectively (Table 1). The hydrodynamic sizes of these NPs were generally smaller in water than in cell culture media, which can be explained by protein adsorption, leading to the formation of protein coronas on the material surfaces [46]. In addition, V_2O_5 and GO NPs displayed negative zeta potentials in DI water, while TiO_2 showed a positive charge in DI water. However, all the zeta potentials reverted to negative charges (−9.4 to −13.4 mV) in cell culture media, as a result of ionic strength and formation of protein coronas.

NP type-specific and cell type-specific cytotoxicity in 2D cultured cell lines

Cell viability in response to ENM exposure was performed first on 2D KC (KUP5) and hepatocyte (Hepa 1–6) cell cultures, using an ATP assay. The result in Fig. 1B demonstrates the impact of ENM-specific effects on cytotoxicity. While V_2O_5 NPs induced significant toxicity in KUP5 as well as in Hepa 1–6 cells in a dose-dependent manner, GO nanosheets showed significant toxicity in KUP5 but not Hepa 1–6 cells. In contrast, TiO_2 had no cytotoxic effects on KUP5 or Hepa 1–6 cells. This indicates the NP type-specific and cell type-specific toxicity profiles in 2D cultured KUP5 and Hepa 1–6 cell lines.

Cellular association and toxic effects of NPs in 3D liver spheroids

To gain insight into potential adverse ENM effects under more physiological conditions, we used the 3D liver spheroids, comprised of Hepa 1–6 and KUP5 cells, for NP exposure. NP uptake and distribution in this 3D culture system were analyzed by optical and fluorescence microscopy. As shown in Fig. 2 A, most ENMs are localized in the vicinity of the outer cell layers, where they could either be attached to the cell surface or taken up. Since it has been shown that the rapidly dissolving V_2O_5 particles can shed potentially cytotoxic pentavalent vanadium ions, V^{5+}, or that GO nanosheets may damage cell viability through cell membrane insertion [37,38], we used an ATP assay to assess particle impact on a combined spheroid cell population. Following exposure to a NP dose range for 16 h, we observed dose-dependent V_2O_5 and GO toxicity, in contrast to only seeing a lesser reduction in cell viability at relatively high TiO_2 doses of 50 and 100 μg/mL (Fig. 2B). In comparison to the results observed in the 2D culture system (Fig. 1B), there was a lesser impact of V_2O_5 or GO particles in the 3D culture system. In addition, we performed a toxicologically relevant functional analysis for an important biomarker for liver injury, aspartate aminotransferase (AST) [47,48]. AST leads to aspartate transamination and is commonly used to survey hepatocyte injury, which leads to leakage of this cytosolic enzyme into the serum [47,48]. While the spheroid exposure to V_2O_5 and GO induced significant AST release, no effect was seen with TiO_2 (Fig. 2 C).

Single-cell RNAseq of 3D liver spheroids after NP treatment

Since no comprehensive studies were undertaken looking at single-cell gene profiling and mechanistic responses in liver spheroids in response to nanoparticles, we used scRNAseq analysis to obtain information about NP- and cell-specific impact on our hanging drop 3D culture system. Guided by the toxicity results in Fig. 2B, a low particle dose of 6.25 μg/mL was used to perform the scRNAseq assessment to keep the cell death rate below 5%. Single-cell suspensions were collected for scRNAseq analysis after spheroid exposure to NPs for 6 h (deliberately chosen to be < 24 h, used in Fig. 2).

After preprocessing and quality control, the scRNAseq analysis was performed on 41,260 cells. Table 2 summarizes the number of Hepa1–6 *vs.* KUP5 cells assembled in each treatment group. Using T-distributed Stochastic Neighbor Embedding (t-SNE) to visualize cell clusters and known genes expressed in each of these cell types, it was possible to positively identify hepatocyte and KCs clusters

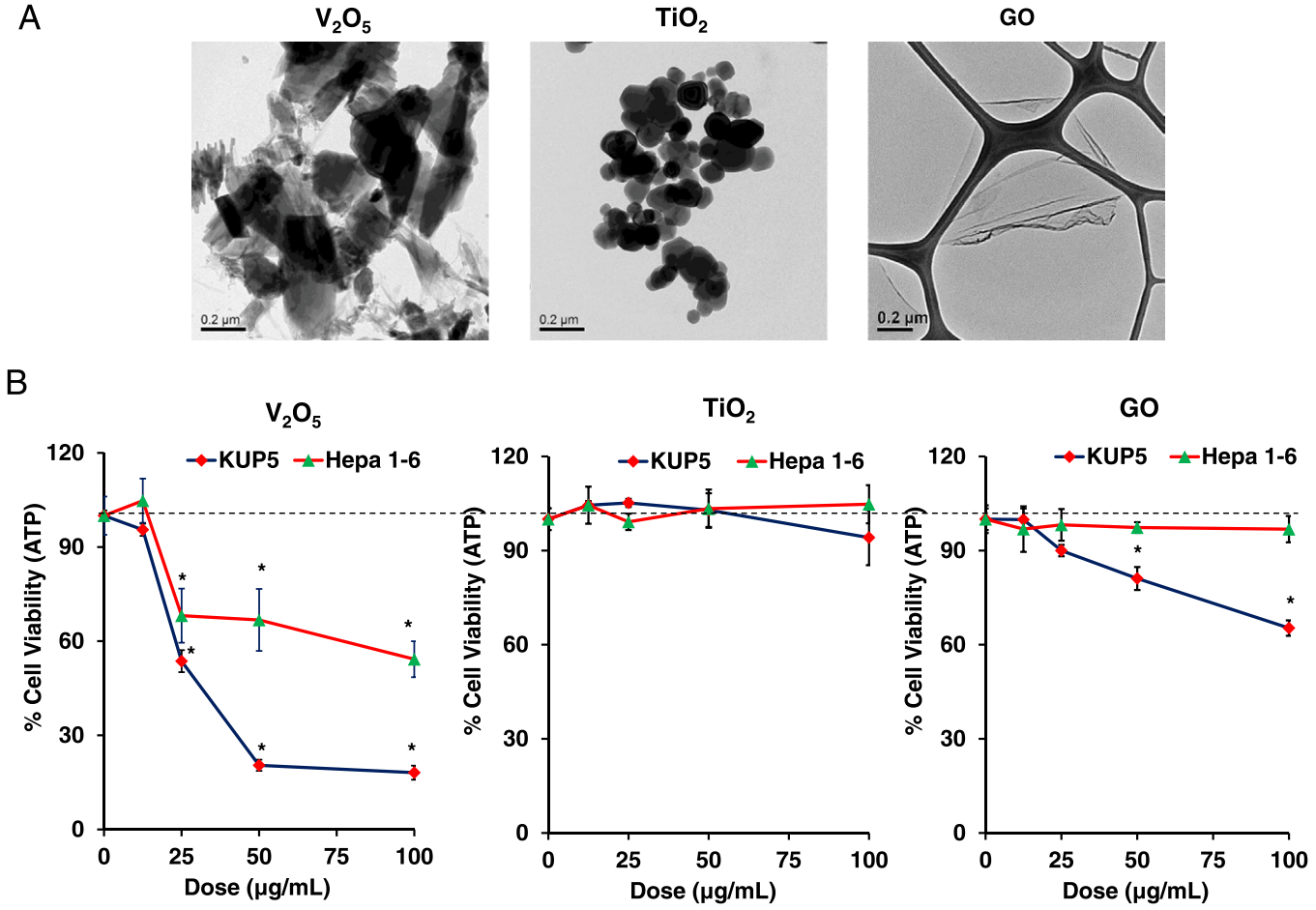

Fig. 1. Characterization of materials in the ENM library. (A) Representative TEM images of V_2O_5, TiO_2, and GO samples obtained by a JEOL 1200-EX TEM with an accelerating voltage of 80 KeV. The scale bar is 0.2 μm. (B) ATP cell viability assay on 2D culture-derived KUP5 and Hepa 1–6 cells after exposure to various NPs at 0 – 100 μg/mL for 24 h. The viability of untreated cells was set as 100%. * represents a p-value < 0.05 compared to the untreated cells.

(Fig. 3A-C). This was further confirmed by assessing hepatocyte-specific biomarkers (Supplemental Fig. 1), towards which we selected albumin (*Alb*), urea secretion (*Ass1, Asl*), CYP450 system (*Cyp1a1, Cyp2e1*), and cellular metabolism (*Ahr, Got1, Apoa2*), as reported previously [25,43,44,49]. We indeed were able to confirm changes in biomarker expression and percentage of cells participating in these responses, in response to nanoparticle treatment. For example, albumin (alb) expression level increased after GO and TiO_2 exposure compared to a decrease after V_2O_5 treatment. There were also changes in urea secretion-related genes such as (*Ass1, Asl*) and cytochrome P450 (*Cyp1a1*). However, these changes are not statistically significant, with the exception of the decrease in albumin and argininosuccinate synthetase 1 (*Ass1*) levels upon V_2O_5 exposure. This is in agreement with the general trend of V_2O_5 being more toxic than other particle types in our analysis.

It is also important to point out that in addition to our *in vitro* scRNAseq analysis, there are voluminous *in vivo* scRNAseq data available in the public database, allowing comparison of cell line data with available information on the mouse and human liver cells. This was accomplished by identifying positive gene markers from our hepatocyte and KCs clusters and comparing them to *in vivo* mouse and human cell type markers (Fig. 3D-E). This analysis revealed a significant overlap between the markers in our study and *in vivo* MCA markers for hepatocytes and KCs in adult mouse livers. Comparison with combined MCA hepatocyte markers showed fold enrichment= 2.4 (p = 7.5e-33) and for Kupffer cell markers, it showed fold enrichment= 11.0 (p = 7.5e-75) (Fig. 3D). Comparison to human scRNAseq data also showed a significant overlap between gene markers from 3D-spheroid cells and the human cell types analyzed from MacParland et al. (GSE115469). For hepatocyte, the comparison with combined human hepatocyte markers showed fold enrichment= 2.6 (p = 1.4e-29). For Kupffer cells, comparison with inflammatory macrophage markers showed fold enrichment= 10.2 (p = 9e-57), and comparison with non-inflammatory macrophage markers showed fold enrichment= 7.7 (p = 5.7e-57) (Fig. 3E). These results show that there are commonalities between our in *vitro* cells and *in vivo* liver cell references [39–45]. In addition, recent studies showed that similar cell types in humans and mice share sufficient

Table 1
Physicochemical characterization of NPs by DLS.

Nanoparticles	Primary size (nm)	Hydrodynamic size (nm)		Zeta potential (mV)	
		DI Water	DMEM	DI Water	DMEM
V_2O_5	380.0 ± 223.1	580.8 ± 45.5	995.1 ± 40.1	-27.3 ± 2.9	-12.4 ± 3.2
TiO_2	125.0 ± 45.7	185.8 ± 7.6	453.7 ± 4.1	36.5 ± 4.7	-13.4 ± 2.3
GO	589.8 ± 340.5	578.6 ± 140.3	623.4 ± 41.9	-40.6 ± 3.8	-9.4 ± 1.0

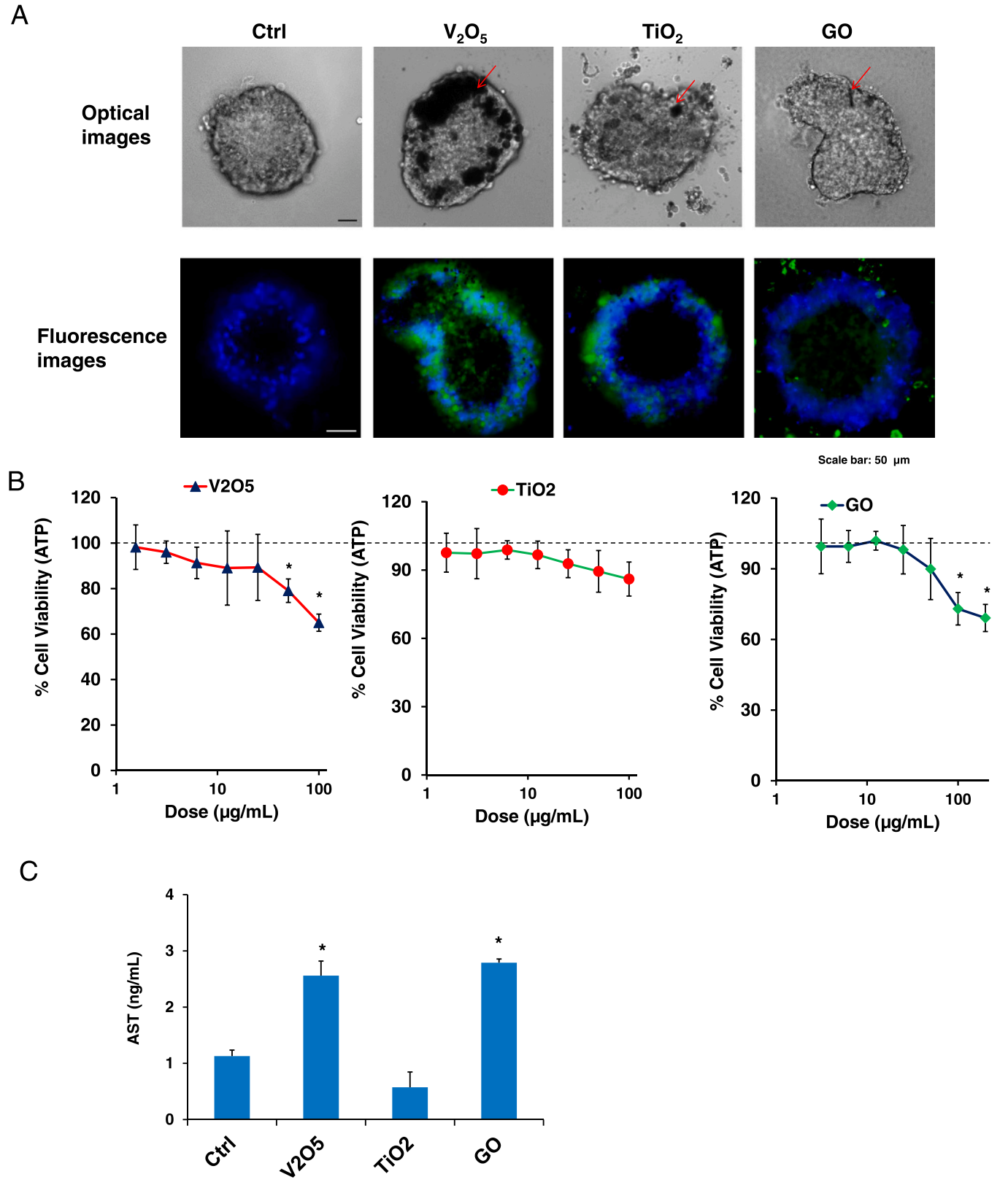

Fig. 2. Determination of cellular association and toxic effects of NPs in the 3D liver spheroids. (A) Optical microscopy and fluorescent images to show the relative abundance of ENM cellular association/uptake of fluorescence-labeled NPs in the different 3D liver spheroids, exposed to 25 μg/mL of the particles for 16 h (red arrows). The scale bar in the image represents 50 μm. (B) Assessment of NP toxicity to the 3D liver spheroids after NP exposure at 0 – 100 μg/mL for 16 h, determined by ATP assay. The viability of untreated cells was set as 100%. (C) 3D liver spheroids were exposed to 25 μg/mL of each ENM suspension. The supernatants were collected for AST quantification. *, p-value < 0.05, indicates a significant difference compared to the control.

Table 2
Summary of the number of differentially expressed genes in the hepatocyte and KC.

Treatment	Total Cell #	Hepatocytes					Kupffer cells (KC)				
		Cell #	Cell %	DEG	Down-reg DEG	Up-reg DEG	Cell #	Cell %	DEG	Down-reg DEG	Up-reg DEG
Control	9868	8508	86.2%	–	–	–	1360	13.8%	–	–	–
V_2O_5	14,563	13,161	90.4%	232	145	87	1402	9.6%	91(141)	6(34)	85(107)
TiO_2	10,009	8447	84.4%	61	52	9	1562	15.6%	16(84)	5(31)	11(53)
GO	6820	6322	92.7%	92	58	34	498	7.3%	6(100)	6(84)	0(16)

Hepatocyte DEG numbers are based on FDR < 0.05. KC DEG numbers are based on FDR < 0.05 and DEG numbers in parenthesis are based on an unadjusted p-value < 0.05.

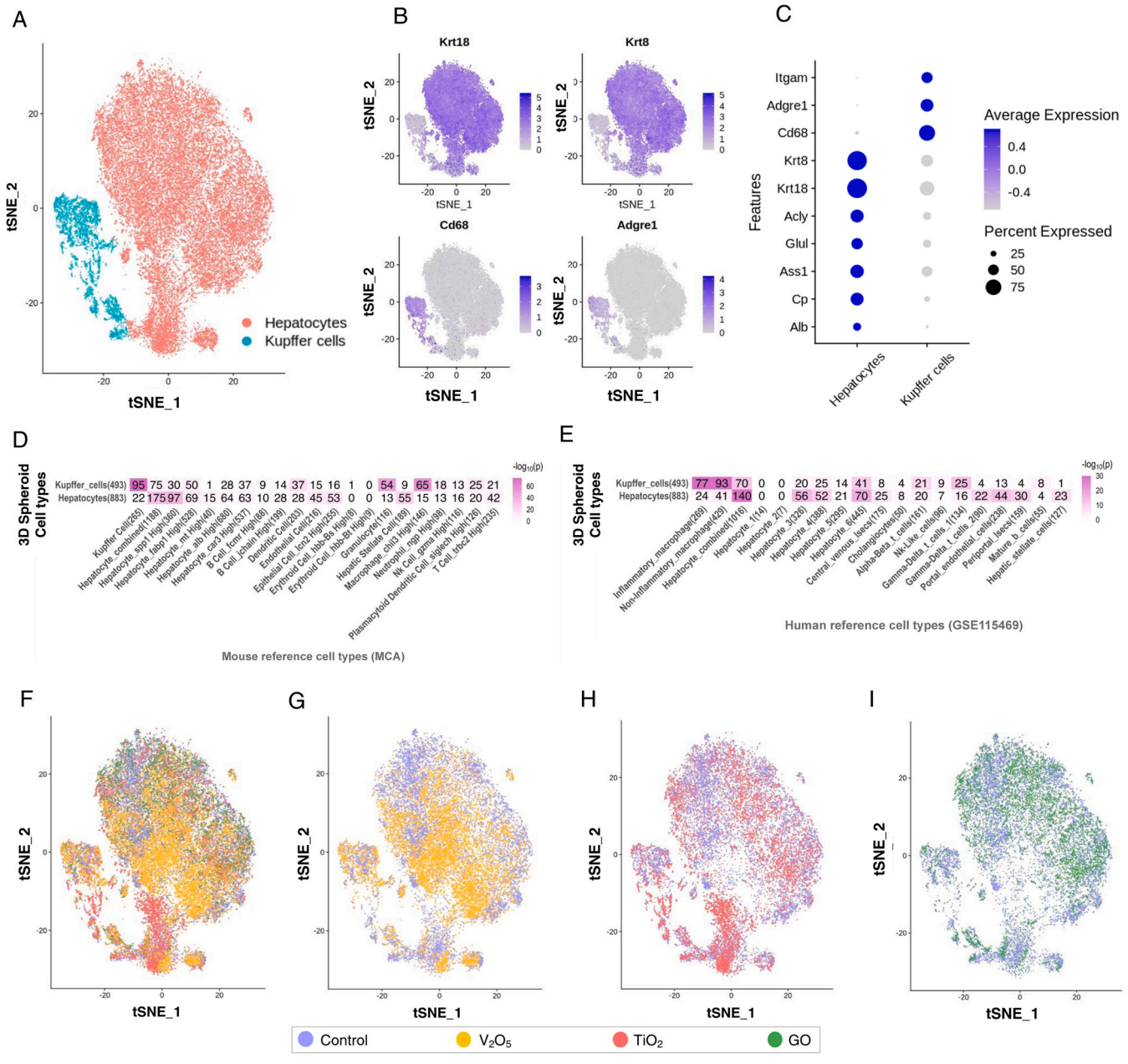

Fig. 3. Cell cluster analysis for hepatocytes and KCs retrieved from liver spheroids following ENM exposure. (A) t-SNE plot showing the identified hepatocyte and KC clusters. (B) t-SNE plot showing hepatocyte and KC marker expression in cell clusters. Each dot represents a cell. (C) Dot plot showing the expression of hepatocyte and KC markers. (D) Heatmap showing the overlaps between 3D spheroid-derived marker genes (y-axis) with mouse liver cell type markers (x-axis) from the Mouse cell atlas (MCA). The Hepatocyte_combined markers represent the collective markers from Hepatocyte_spp1 High, Hepatocyte_fabp1 High, Hepatocyte_mt High, Hepatocyte_alb High, and Hepatocyte_car3 High clusters. (E) Heatmap showing the overlaps between 3D spheroid-derived marker genes (y-axis) with human liver cell type markers (x-axis) obtained using MacParland et al. (GSE115469) dataset. The Hepatocyte_combined markers represent the collective markers from Hepatocyte_1 – Hepatocyte_6 clusters. The number of marker genes for each cell type is indicated in the parenthesis. The number of overlapping marker genes is shown in the cells. The statistical significance of marker overlap was determined using Fisher's exact test and indicated by color (the darker color indicates higher significance). (F-I) t-SNE plot showing the cells that originated from the different treatment groups (F) with blue cells originating from control, yellow cells from vanadium pentoxide (V_2O_5) treated spheroids (G), red cells from titanium dioxide (TiO_2) treated spheroids (H), and green cells from graphene oxide (GO) treated spheroids (I).

gene expression signatures to integrate scRNAseq data between the two species in the liver [50] and other organs or tissues [51–54]. The high level of similarities between mice and human raises the potential of utilizing the scRNAseq data from mice to predict the toxicological responses of humans. Furthermore, our experiment using mouse cells provide a good opportunity for comparison between *in vitro* mouse spheroids and *in vivo* mouse models to study the effects of nanomaterials on the liver (*in vivo* study in the future), while *in vivo* human studies are much less feasible.

Among the 41,260 cells in the study, there were 36,438 hepatocytes and 4,822 KCs, which is roughly similar to the 9:1 ratio in which hepatocytes and KCs are combined for spheroid construction. Among the three nanomaterials, TiO_2 was most similar in maintaining a cell ratio that is equivalent to control cells. In contrast, V_2O_5 and GO treatment increased the ratios of hepatocytes to KC (Table 2). This is in keeping with the more pronounced impact of V_2O_5 and GO on KC viability, as demonstrated in the cytotoxicity analysis (Figs. 1B and 2B).

NP type-specific gene expression and pathway changes in hepatocytes of 3D liver spheroids

Using t-SNE treatment plots, V_2O_5 exposed cells showed the biggest deviation from the control cells (Fig. 3F-I), indicating broader transcriptomic changes. In hepatocytes, V_2O_5 had the largest number of DEGs (232), followed by GO (92 DEGs) and then TiO_2 (61 DEGs) (Table 2, Fig. 4A-C, full list of DEGs in Supplemental Table 4). This order agrees with the hepatocyte toxicity data both in 2D and 3D culture systems (Fig. 1B and Fig. 2B), suggesting consistency between gene-level and phenotype data. We also compared the DEGs between the different ENMs. Although some genes were shared between any two NPs, there was no genes shared among all three ENMs used in this study (Fig. 4D). Thus, the majority of the DEGs were specific to each material, indicating the ENM-specific gene expression changes for spheroid-derived hepatocytes.

To validate the biological basis for the DEGs related to each ENM, we performed a pathway enrichment analysis. V_2O_5-treated hepatocytes showed enrichment in pathways commensurate with NF-κB-mediated TNF-α signaling, apoptosis responses, pro-inflammatory gene expression, TOLL-like receptor (TLR) signaling, and TGF-β1 pathways (Fig. 4E). The full list of pathways is summarized in Supplementary Table 5. Hepatocytes recovered from TiO_2-treated spheroids demonstrated that the principal enriched pathways are indicative of NF-κB-mediated TNF-α signaling, p53 signaling, hypoxia pathways, TOLL receptor cascades, and TGF-β1 signaling (Fig. 4F), with the full list of pathways appearing in Supplementary Table 5. In the case of GO, the principal response pathways in hepatocytes appear to be related to iron uptake and transport, oxidative phosphorylation, NF-κB-mediated TNF-α signaling, TLR signaling, and NOD-like receptor signaling (Fig. 4G), with the full list appearing in Supplementary Table 5.

We also asked whether there was an impact of nanoparticles on unique or shared pathways in hepatocytes. Despite the lack of common DEGs among the ENMs, there was some NF-κB and TOLL-related pathway shared among the materials, with a suggestion of also involving TNF-α signaling (Supplementary Table 6). NP-specific pathways in hepatocytes were also identified for V_2O_5 (*e.g.*, adipogenesis and cholesterol homeostasis), TiO_2 (*e.g.*, innate immune system and pyruvate metabolism), and GO (*e.g.*, iron uptake and transport, respiratory electron transport, and the chemokine signaling pathway) (Supplemental Table 6). Overall, the trend is towards hepatocyte pathways related to inflammation and cell death, reminiscent of the demonstration of tiered oxidative stress response pathways, described in 2D cultures.

NP type-specific gene expression and pathway changes in KCs of 3D liver spheroids

In KCs, using an FDR < 0.05 threshold, V_2O_5 (91 DEGs) demonstrated the highest number of DEGs, followed by TiO_2 (16 DEGs) and GO (6 DEGs) (Table 2 and Fig. 5A-C). Compared to hepatocytes, there were fewer DEGs in KCs, which could be due to the recovery of lower cell numbers, which limits the identification of DEGs (Table 2). Because of the lower number of DEGs identified in KCs at FDR < 0.05, we also evaluated unadjusted p-value < 0.05, resulting in 141, 84, and 100 genes for V_2O_5, TiO_2, and GO, respectively (Table 2, Fig. 5A-C), with the full list appearing in Supplementary Table 7. When comparing the genes from all three nanoparticles at a $p < 0.05$ threshold, there were four shared genes, *Tulp4*, *Fam162a*, *Il1b*, and *Malat1* (Fig. 5D and Supplementary Table 7). The relationship of *Fam162a* and *Il1b* to apoptosis suggests that cell death pathways may be targeted by all three ENMs in KCs.

The enriched pathways in KC, treated with V_2O_5, included NF-κB-mediated TNF-α signaling, p53 signaling, oxidative phosphorylation, and xenobiotic metabolism, while for TiO_2, the major impact was on NF-κB-mediated TNF-α signaling, p53 signaling, NGF signaling, and respiratory electron transport pathways. For GO, the enriched pathways included NF-κB-mediated TNF-α signaling, p53 signaling, apoptosis, and MTORC1 signaling pathways (Fig. 5E-G), with the full list of pathways appearing in Supplementary Table 8. An analysis of KC pathways shared amongst all NPs, included p53 signaling, hypoxia, and TNF-α signaling *via* NF-κB. Among the pathways that are unique for each nanomaterial, we observed: V_2O_5 impact on a xenobiotic pathway engaged in chemical detoxification and protection; TiO_2 impact on insulin, PPARA, and IL-2 pathways; and GO impact on cholesterol homeostasis and MTORC1 signaling (Supplemental Table 6). All considered, the above data indicate that all three ENMs could exert an impact on pro-inflammatory responses *(e.g.*, TNF- α *via* NF-κB) and cell death pathways (*e.g.*, p53 signaling, apoptosis) in KCs.

Pathway analysis to compare the gene expression profiles of hepatocytes with KCs obtained from spheroids

We compared the DEGs and pathways of hepatocytes and KCs to see if there were differential responses to NP exposure (Supplemental Fig. 2). In V_2O_5 treated spheroids, there were 53 common DEGs between hepatocytes and KCs (*e.g.*, *Ctsk, Rpl6, Eif3j1, mt-Nd3, and Serbp1*), 179 hepatocyte-specific DEGs (*e.g.*, *Slc1a2, Wnt6, Btg2, Cyb5a, and Saa3*), and 88 KC-specific DEGs (*e.g.*, *Spp1, Malat1, Dab2, Rps16, and Slc6a12*) (Supplemental Fig. 2A). At the pathway level (Supplemental Table 9), V_2O_5 triggered glycolysis, cholesterol homeostasis, apoptosis, and MTORC1 signaling pathways in hepatocytes, while impacting genes involved in granulocyte function, oxidative phosphorylation, TCA cycle, and the respiratory electron transport chain in KCs. Pathways common to hepatocytes and KCs included aspects of xenobiotic metabolism, TOLL-like receptor signaling, p53 signaling, and TNF-α signaling *via* NF-κB. V_2O_5 induced significant changes in metabolic and pro-inflammatory pathways in both cell types, although there are many differences in specific pathway changes.

For TiO_2 treatment, there were 9 common genes between hepatocytes and KCs (*e.g.*, *Fos, Jun*, *Btg1*, *Hspa4l*, and *Hif1a*), 52 DEGs unique to hepatocytes (*e.g.*, *Fosb*, *Sprr1a*, *Dusp1*, *Tcim*, and *Nupr1*), and 75 DEGs uniquely altered in KCs (*e.g.*, *Ptgs2*, *Il1rn*, *Nos2*, *Lgals1*, and *Lars2*) (Supplemental Fig. 2B). At the pathway level, the changes in hepatocyte-specific pathways included pyruvate metabolism and innate immune system pathways, while the KC-specific pathways included apoptosis and oxidative phosphorylation. Common pathways found in both the hepatocytes and KCs were TNF-α signaling

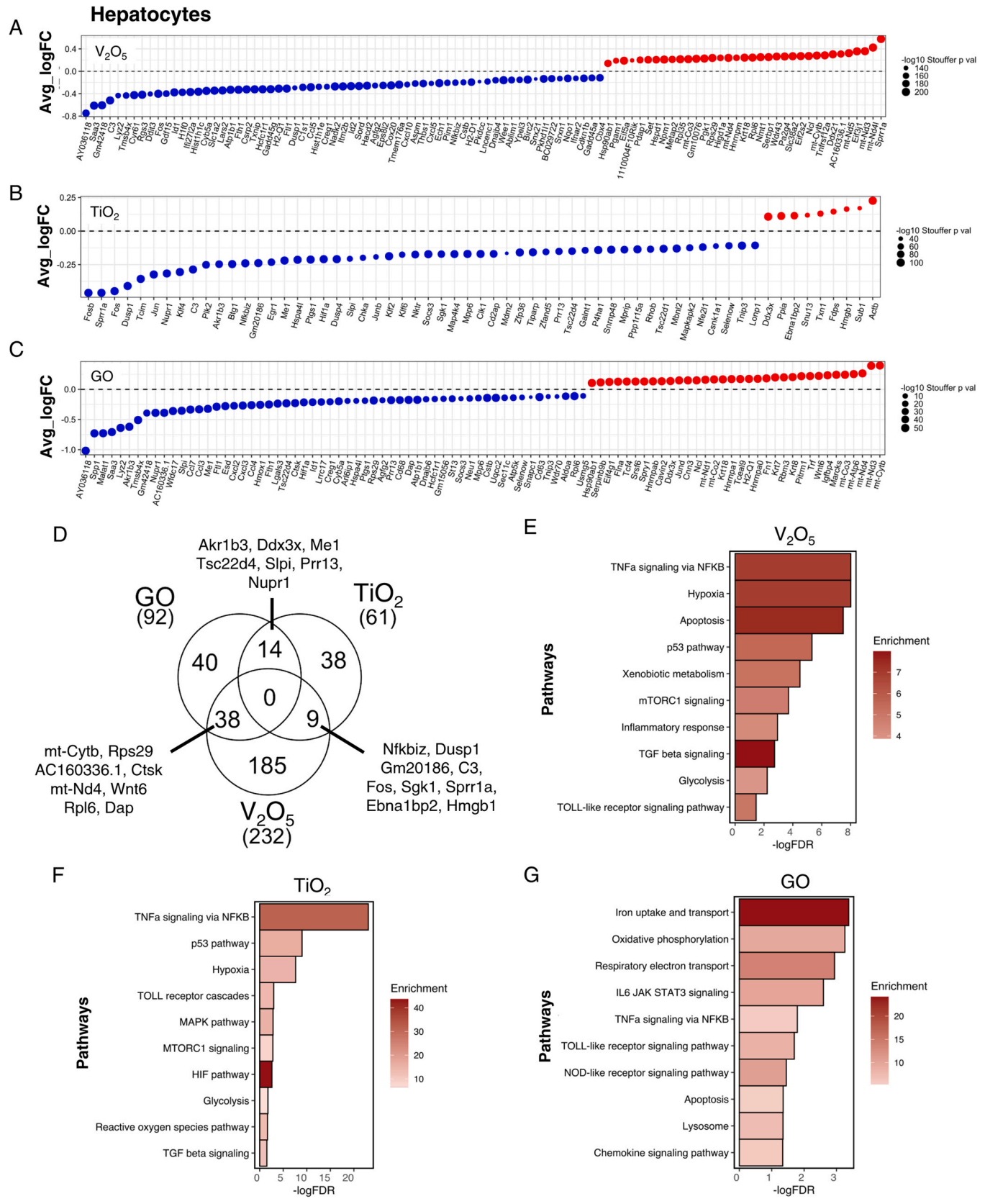

Fig. 4. Analysis of differentially expressed genes (DEGs) and enriched pathways in spheroid-derived hepatocytes, following NP exposure. (A-C) Dot plot of DEGs induced by vanadium pentoxide (V_2O_5) (A), titanium dioxide (TiO_2) (B), and graphene oxide (GO) (C) in hepatocytes. The DEGs used for this analysis had an FDR < 0.05. The size of each dot is proportional to the -log10 (Stouffer's combined p-value) and the max was set to 200, 100, and 50 for V_2O_5, TiO_2, and GO, respectively. The color of the dots corresponds to the direction of averaged log fold change (FC), with red representing upregulated genes and blue representing downregulated genes. (D) Venn diagram comparing DEGs for V_2O_5, TiO_2, and GO. (E-G) Bar plot of the enriched pathways obtained by V_2O_5 (E), TiO_2 (F), and GO (G) treatment of hepatocytes. The DEGs used for the pathway analysis had an FDR < 0.05 and pathways considered significant had an FDR < 0.05. (E-G). The size of the bars is proportional to the -log (FDR). Color corresponds to the enrichment score.

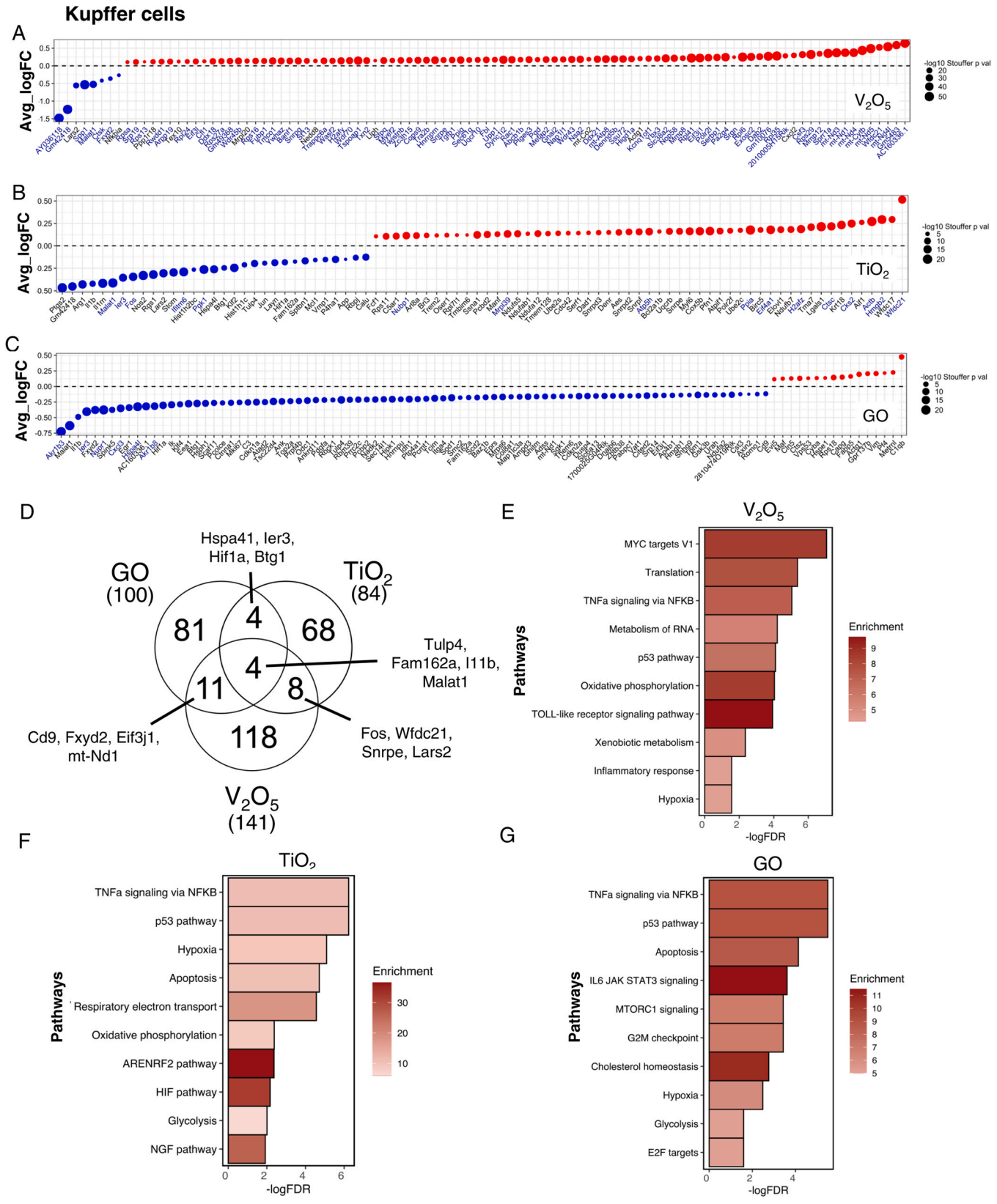

Fig. 5. Differentially expressed genes (DEGs) and enriched pathways in response to exposure in spheroid-derived KCs. (A-C) Dot plot of DEGs induced by vanadium pentoxide (V_2O_5) (A), titanium dioxide (TiO_2) (B), and graphene oxide (GO) (C). DEGs shown had an unadjusted p-value < 0.05. Genes with blue text color represent those that also had an FDR < 0.05. The size of each dot is proportional to the average -log10 (Stouffer's combined p-value) and the max was set to 50 for V_2O_5 and then 20 for both TiO_2 and GO. The color of the dots corresponds to the direction of change in the log fold (FC) average, with red representing upregulated genes and blue representing downregulated genes. For V_2O_5 (A) only the top 100 genes based on the average -log10 (Stouffer's combined p-value) are plotted. (D) Venn diagram comparing the number of DEGs between V_2O_5, TiO_2, and GO. The DEGs compared had an unadjusted p-value < 0.05. (E-G) Bar plot of the enriched pathways affected after V_2O_5 (E), TiO_2 (F), and GO (G) treatment. The DEGs used for the pathway analysis had a p-value < 0.05 and pathways that were considered significant had an FDR < 0.05. The size of the bar is proportional to the -log (FDR). Color corresponds to the enrichment score.

via NF-κB, insulin, glycolysis, and hypoxia pathways (Supplemental Table 9). Interestingly, TiO_2 affects mitochondrial metabolism and oxygen sensing pathways in addition to pro-inflammatory and cell death pathways, which is very different from the V_2O_5 effects.

After exposure to GO, there were 10 common DEGs between hepatocytes and KCs (*e.g.*, *Malat1*, *Akr1b3*, *Nupr1*, *Cxcl3*, and *Tsc22d4*), 82 DEGs uniquely altered in hepatocytes (*e.g.*, *Spp1*, *Saa3*, *Lyz2*, *Tmsb4x*, and *Wfdc17)*, and 90 DEGs uniquely altered in KCs (*e.g.*, *Odc1*, *Akr1b8*, *Ier3*, *Cdkn1a*, and *Mrps6*) (Supplemental Fig. 2C). At the pathway level, the hepatocytes had enriched pathways related to iron uptake and transport and oxidative phosphorylation pathways, while the KCs had pathways related to glycolysis and cholesterol homeostasis. Common pathways in hepatocytes and KCs in GO were apoptosis and TNF-α signaling *via* NF-κB (Supplemental Table 9). Different from TiO_2 and V_2O_5, GO shows effects on pathways involved in iron uptake in hepatocytes and cholesterol homeostasis in KCs, showing different ENMs could induce unique changes.

The above results indicate the cell-type-specific gene expression and pathway changes in various NPs-treated 3D liver spheroid, although a limited number of common genes and pathways are shared between cell types (*e.g.*, pro-inflammatory and apoptotic pathways) in each case.

Effects of NP treatments on cell-type subclusters in 3D liver spheroids

Within the two liver cell types, there were also different subclusters among hepatocytes (5 subclusters, named hepatocytes1–5) and KCs (3 subclusters, named KC1–3), which each had unique expression patterns (Fig. 6A and B). In the evaluation of the gene expression changes in the hepatocyte and KC subclusters during NP exposure, we observed that the cluster designated Hepatocytes1, showed the highest number of DEGs when using a threshold of FDR < 0.05 (Table 3), with the full list of DEGs appearing in Supplementary Table 10. This finding is likely due to the statistical strength of more than half of the treated cells consisting of hepatocytes (Fig. 6 A and Table 3). In the KC subclusters, KC1 one showed the highest number of DEGs (Table 3), with a full list of DEGs appearing in Supplementary Table 10.

Pathway enrichment analysis was also conducted among the identified DEGs, with the caveat that the analysis was conducted in the subclusters, where there were at least 50 DEGs identified with an unadjusted p-value < 0.05 (Full list of pathways in Supplemental Table 11). In V_2O_5-treated spheroids, an apoptosis pathway was shared by 4 out of the 5 hepatocyte subclusters (Fig. 6 C). Xenobiotic metabolism and TGF-β1 signaling pathway were only observed in Hepatocytes1 and IL-7 and bile acid metabolism was identified only in Hepatocytes2. In the two KC subclusters with > 50 DEGs, a shared, TLR signaling pathway was discerned (Fig. 6 C). Pathways such as angiogenesis and hypoxia were found in only the KC1 subcluster, while p53 signaling was only enriched in KC2 (Fig. 6 C). This further confirms the cell-type-specific pathways in V_2O_5-treated 3D liver spheroids. Despite the differences, most shared pathways involve inflammation or apoptosis in both cell types.

In TiO_2-treated 3D spheroids, the insulin signaling pathway involved in glycogen synthesis and lipid production was shared between Hepatocytes1 and Hepatocytes3 subclusters (Fig. 6D). However, TNF-α signaling *via* NF-κB, PPAR-α signaling, and hypoxia were among the pathways only enriched in hepatocytes1, and RNA metabolism was only observed in hepatocytes3 (Fig. 6D). Pathway enrichment for both KC1 and KC2 included changes in genes involved in glycolysis and hypoxia (Fig. 6D). There were also unique pathways within the two KC clusters: xenobiotic metabolism was unique to KC1 and pathways such as reactive oxygen species and oxidative phosphorylation were observed only in KC2 (Fig. 6D). For TiO_2, oxidative stress and pro-inflammatory but not cell death pathways were the most common in hepatocytes and KCs.

For GO treatment, Hepatocytes1 and 5 subclusters shared pathways such as iron uptake and transport, oxidative phosphorylation, TCA cycle and electron transport (Fig. 6E). However, NF-κB-related TNF-α signaling was only enriched for Hepatocytes1 and KREB pathway was only observed in Hepatocytes5 (Fig. 6E). Among the KC subclusters, only KC1 displayed more than 50 DEGs, indicating pathway enrichment for MTORC1 signaling, lysosome function, and cholesterol homeostasis (Fig. 6E). Overall, GO differs from V_2O_5 and TiO_2 insofar as its gene profiling in being more related to aspects of metabolic function.

3.9. Validation of NP-induced ROS generation in mitochondria

From an overall perspective, scRNAseq analysis revealed cellular responses that are compatible with the tiered oxidative stress response pathway, involving pro-inflammatory, and cell death response pathways, as described earlier.[5.19,20]. Since toxic oxidative stress can induce cell death *via* mitochondrial effects, it is relevant that we observed evidence of changes in *mt-Cytb* and *mt-Nd4* genes that are involved in mitochondrial respiratory electron transport and ROS signaling (Fig. 4). To confirm the gene response pathways by more conventional cellular assays, we used the MitoSOX Red fluorescence staining to assess mitochondrial ROS (mtROS) production. This indicated a significant increase in fluorescence intensity in spheroid cells following exposure to V_2O_5 or GO compared to the control or TiO_2 (Fig. 7 A). Quantification for fluorescence intensity in a microplate reader further confirmed that mtROS production in the V_2O_5 or GO-treated spheroids increased 66.8 ± 10.4% and 36.3 ± 19.6%, respectively, compared to the control, with V_2O_5 dominating over GO (Fig. 7B). These results were consistent with the cytotoxicity data in Fig. 2B and findings in Figs. 4 and 5 that are compatible with oxidative stress and apoptosis-related gene expression.

Validation of NP-induced caspase-1 activation and pro-inflammatory response pathways in 3D liver spheroids

The demonstration of increased *Nupr1* gene expression during scRNAseq analysis of hepatocytes exposed to TiO_2 and GO, suggests the potential involvement of pro-inflammatory responses that have been linked to caspase-1 cytotoxicity pathways (Fig. 4) [47]. This includes the linkage of caspase-1 to liver cell responses that have been linked to interleukin-1β (IL-1β) and IL-18 release [48]. This prompted us to assess caspase-1 activation, using fluorescent microscopy to observe the cleavage of the enzyme-substrate, FAM-YVADFMK. Fig. 7 C demonstrates increased caspase-1 activation by V_2O_5 or GO NPs, compared to the control or TiO_2 nanoparticles. This was also confirmed by quantification of the response in a microplate reader, showing that V_2O_5 and GO NPs, could increase the signal by 133.6 ± 20.5% and 31.1 ± 16.5%, respectively, compared to the control (Fig. 7D). The response to V_2O_5 was significantly stronger than for GO. These results are consistent with the cytotoxicity data in Fig. 2B, as well as evidence of the involvement of the inflammasome pathways in the sequencing data displayed in Fig. 4 and Fig. 5 C.

Validation of ENM-specific cytokine production in 3D liver spheroids

Caspase-1 activation in the context of the NRLP3 inflammasome is involved in pro-IL-1β cleavage and the release of mature IL-1β [38]. This is compatible with the data in Supplemental Table 7, which include evidence of IL-1β gene expression in response to NP

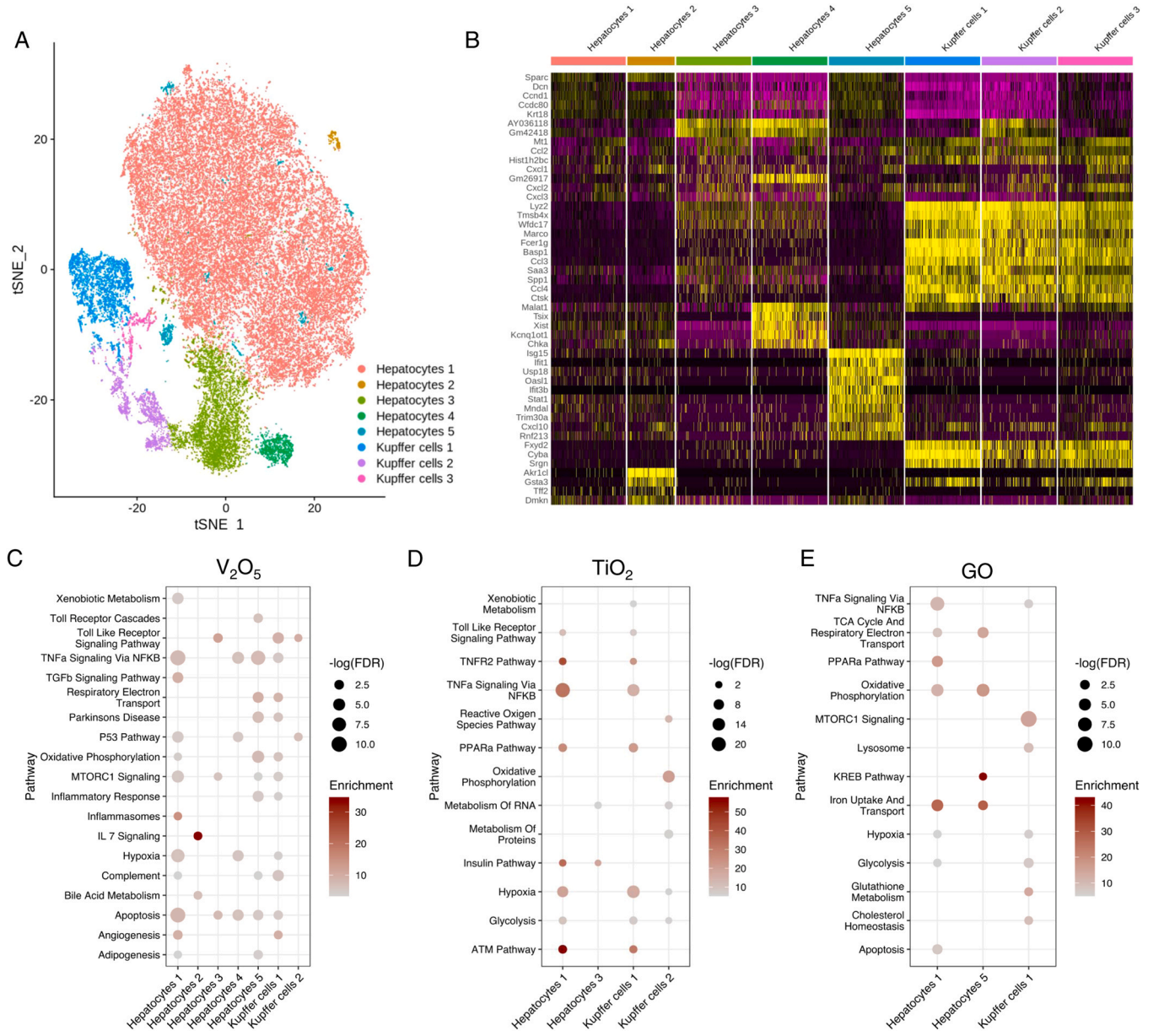

Fig. 6. Hepatocyte and KC subcluster analysis and enriched pathways, following NPs exposure of 3D liver spheroids. (A) The t-SNE plot of hepatocyte and KC subclusters. (B) Heatmap of the top 10 markers of the hepatocyte and KC subclusters. (C-E) Dot plot of the enriched pathways obtained following V_2O_5 (C), TiO_2 (D), and GO (E) exposure. Pathways that were considered significant had an FDR < 0.05. Pathway enrichment was only done when there were at least 50 DEGs at a p-value < 0.05. The size of each dot is proportional to the -log (FDR). The color of the dots corresponds to the enrichment score.

treatment of the liver spheroids. This prompted us to use an ELISA for measuring IL-1β release from liver spheroids, following ENM exposure. As shown in Fig. 8A, the secretion of IL-1β was increased by 79.3 ± 12.7% and 42.8 ± 7.4% in response to V_2O_5 and GOs, respectively, without significant change for TiO_2 in relation to the control. Also, V_2O_5 NPs induced significantly stronger IL-1β release than GO NPs, consistent with the caspase-1 activation data.

In addition to the impact on IL-1β, our scRNAseq data demonstrated significant changes in the expression levels of TNF-α (Supplementary Table 10) and TGF-β1 (Supplementary Table 7) pathway related genes, including evidence for the involvement of NF-κB and the TGF-β1 signaling pathways in response to NP treatment (Fig. 4). We, therefore, used ELISA kits to measure TNF-α and TGF-β1 release in the supernatants of liver spheroid cells after NP treatment. As shown in Fig. 8B, TNF-α production was increased by 42.3 ± 2.8% and 91.0 ± 9.4%, respectively after GO and TiO_2 treatment, without significant change in response to V_2O_5 NPs. Moreover, Fig. 8C demonstrates that the secretion of TGF-β1 increased by 117.8 ± 19.7% and 170.3 ± 24.0% for V_2O_5 and TiO_2 NPs, respectively, without change for GO NPs.

Discussion

In this study, we used a 3D culture system and state-of-the-art scRNAseq high throughput technology to perform a comparative study of gene changes that may be indicative of toxicological responses in Kupffer cells and hepatocytes to exposure to different ENMs, V_2O_5, TiO_2 and GO. The results demonstrate ENM- and cell-

Table 3
Summary of the number of differentially expressed genes in the hepatocyte and KC subclusters.

Cell type	Subcluster		Control	V_2O_5	TiO_2	GO
Hepatocytes	1	Cell %	70.4	80.9	55.8	83.6
		DEG	–	231 (237)	48 (52)	99 (101)
	2	Cell %	0.5	0.5	0.3	0.6
		DEG	–	0 (105)	0 (13)	0 (21)
	3	Cell %	10.7	5.2	25.7	5.9
		DEG	–	11 (66)	4 (100)	4 (32)
	4	Cell %	3	2.8	1.2	0.9
		DEG	–	0 (175)	0 (21)	0 (18)
	5	Cell %	1.7	1.3	1.1	1.7
		DEG	–	1 (219)	0 (36)	0 (58)
Kupffer cells	1	Cell %	7.6	6.9	7.1	3.5
		DEG	–	63 (176)	22 (96)	1 (87)
	2	Cell %	5.3	1.3	6.4	3.8
		DEG	–	3 (60)	2 (93)	0 (44)
	3	Cell %	0.8	1.1	2.5	0.1
		DEG	–	0 (29)	0 (16)	0 (0)

Hepatocyte and KC DEG numbers are based on FDR < 0.05. The number of DEGs that meet the p-value < 0.05 threshold are shown in parentheses.

specific responses in liver spheroids, including response profiling indicative of pro-inflammatory and cell death pathways commensurate with a hierarchical oxidative stress response pathway. Overall, spheroid-derived hepatocytes showed the largest number of changes in gene expression, suggesting that these cells are more responsive to ENM effects on metabolic, inflammatory, and apoptosis response pathways. In addition, the changes in gene expression were accompanied by ENM-specific effects on mtROS generation, caspase-1 activation, and the release of IL-1β, TNF-α, and TGF-β1. Moreover, there were significant differences in the responses of hepatocyte *vs*. Kupffer cells in relation to different ENMs, providing valuable information on the range of adverse outcomes in the cells under 3D culture conditions, which mimic the intact liver architecture. These findings can assist biomarker development to assess nanomaterial impact on the liver, including for nanomaterial safety assessment of nano-enabled biopharmaceuticals.

The key finding in this study is the delineation of the toxicological response pathways to three nanomaterials in liver spheroids, utilizing scRNAseq expression profiling. This corroborates previous studies showing that 3D cell culture models can be used for mimicking the complexity of cell-to-cell interactions under *in vivo* conditions [19–21]. Moreover, 3D cultures allow the study period to be extended for weeks, thereby allowing long-term and repetitive exposure to potential toxicological stimuli, including ENMs. The spheroid model also allows the study of cell-cell and cell-matrix interactions, which are better captured during the use of scRNAseq technology, to distinguish responses in individual cell types [20,22–25].

In our data analysis, we identified 5 hepatocyte and 3 KC subtypes of KCs through the use of scRNAseq technology. The spatial arrangement of cells in the inner and outer layers of the liver spheroid 3D architecture allowed a gradient of different exposure conditions to the NP used in the study. Moreover, the range of hepatocyte-to-hepatocyte, hepatocyte-to-KC, and KC-to-KC interactions impact gene expression and signaling pathways that better mimic intercellular communication in the intact liver microenvironment [16,48]. For example, the "janitorial" function of KCs can help to preserve hepatocytes from being damaged by cellular debris or particulate matter through phagocytosis, and degradation of these potential noxious stimuli [55].

The use of scRNAseq analysis provides detailed information about the complicated molecular interactions between multiple cell types in intact tissues as well as 3D liver spheroids, as demonstrated in the study [28,56–59]. This also allowed us to identify hepatocyte- and KC-specific changes in gene expression profiling during NP exposure (*i.e.*, V_2O_5, TiO_2, and GO), with inferences about differences in the toxicological pathways. For instance, while TiO_2 did not result in any significant cytotoxic effects in hepatocytes and KCs, the sensitivity of scRNAseq analysis allowed the capture of the gene and pathway responses that could not be discerned by cytotoxic assays alone. Interestingly, most of these non-lethal changes involved evidence of TiO_2-induced oxidative stress and inflammation. Not only did this involve TLR responses to TiO_2 in hepatocytes, but we could also demonstrate TLR effects for V_2O_5 and GO in the cells. TLRs play an important role in triggering innate immune responses and cytokine production [60]. In this regard, GO nanosheets have previously been shown to engage TLR4 and TLR9 response pathways, leading to pro-inflammatory responses and autophagy [61]. Another pathway engaged by all three NPs in hepatocytes or by GO and TiO_2 in the KCs was the triggering of TNF-α production, which is known to play a role in hepatitis [62,63]. Noteworthy, we could also show that engagement of pro-oxidative and inflammatory pathways according to scRNAseq analysis, could be validated by conventional assays showing evidence of TNF-α and TGF-β1 production; TGF-β1 plays a role in the development of tissue inflammation and fibrosis [64–67].

Dosimetry is a critical factor to consider for any toxicological studies. Although there are *in vitro* and *in vivo* animal data available, human data is not actively available, including the liver. The current best-studied nanomaterial *in vivo* dosimetry model is physiologically based pharmacokinetic modeling (PBPK). However, the PBPK models so far only have limited success due to the different physicochemical properties of nanomaterials (size, charge, shape, hydrophobicity/hydrophilicity), protein corona, and the RES systems that can significantly alter the nanomaterials' PK and TK. Despite the lack of *in vivo* data to extrapolate the *in vitro* dosimetry, the consensus is the doses in most *in vitro* studies are considered high, which is more representative of long exposure times [6,7]. Despite shortcomings in the high *in vitro* doses, *in vitro* assays still, give highly relevant information on toxicity mechanisms that are informative of what happens *in vivo* and in humans [5]. The key contribution of this study is that it offers efficient and effective approaches and high-resolution cell-type-specific molecular insights for assessing the impact of nanomaterials on the liver, which is useful for comparison with *in vivo* animal results or human results when available.

In summary, we used the 3D liver model as a tool to evaluate the interactions between hepatocytes and KCs that better mimic *in vivo* settings and the critical functional changes in response to NP exposure. Furthermore, scRNAseq analysis could also elucidate toxicological response pathways to different NPs and liver cell types at a more sensitive level than conventional screening technology. This

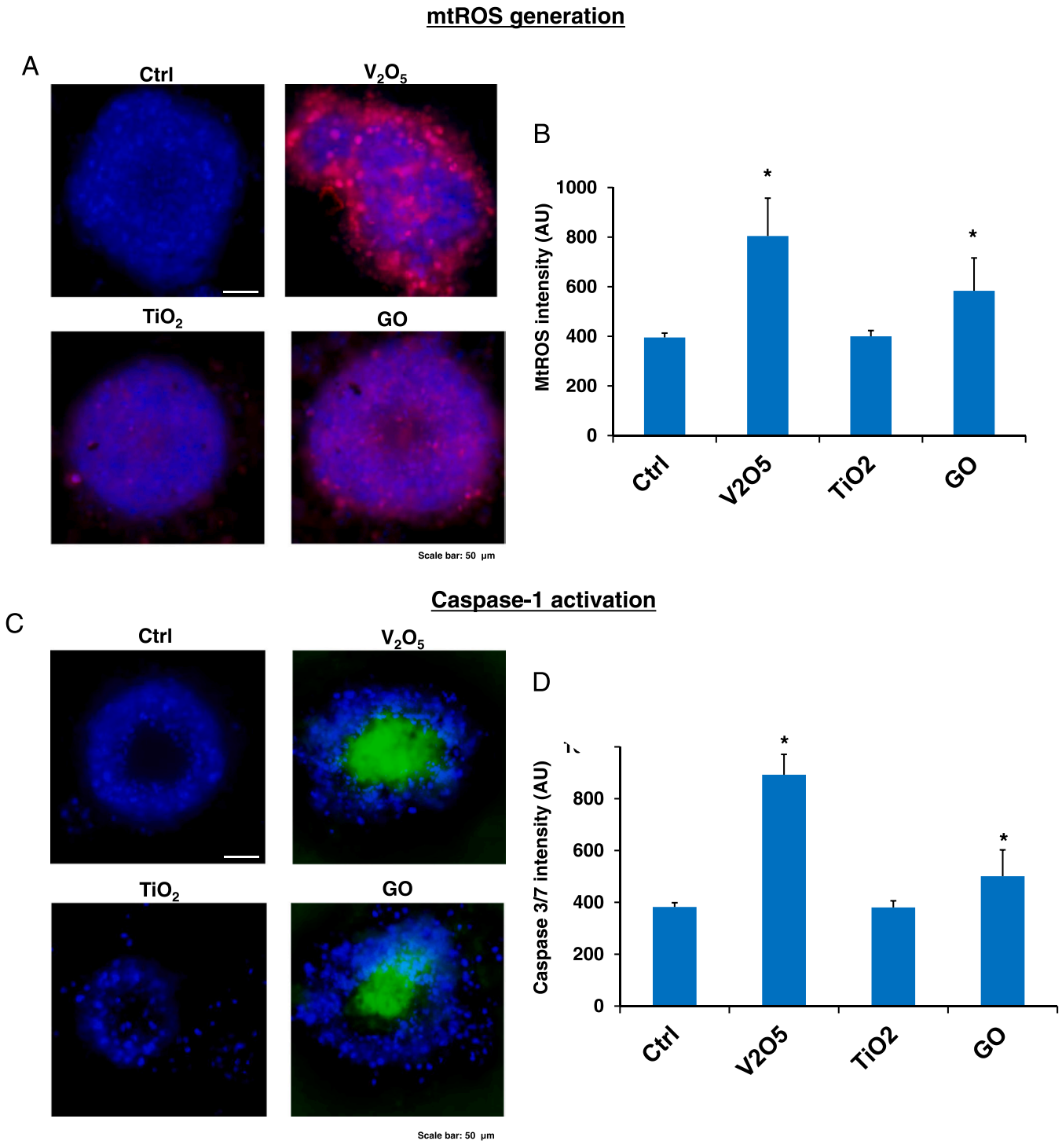

Fig. 7. Confirmation of apoptotic and inflammatory pathways in 3D liver spheroids. (A) Fluorescent images to determine mtROS generation by various NPs in 3D liver spheroids. Liver spheroids were exposed to 25 μg/mL of the materials for 16 h, before staining with 5 μM MitoSOX red for 15 min in HBSS, followed by staining with Hoechst 33342 (blue) for 45 min. The scale bar represents 50 μm. (B) Quantification of mtROS generation in liver spheroids in a microplate reader. The fluorescence intensity was detected at excitation/emission wavelengths of 510/580 nm. * represents a p-value < 0.05 compared to the untreated control. (C) Fluorescent images to determine caspase-1 activation by various NPs in 3D liver spheroids. Liver spheroids were exposed to 25 μg/mL of the materials for 16 h, before staining with the FAM-FLICA caspase-1 substrate (green) for 1 h and then with Hoechst 33342 (blue) for 30 min. The scale bar represents 50 μm. (D) Quantification of caspase-1 activation in liver spheroids using a microplate reader. The fluorescence intensity was monitored at excitation/emission wavelengths of 492/520 nm. * represents a p-value < 0.05 compared to the untreated control.

implies that the use of scRNAseq technology in 3D liver models could provide a more sensitive and high throughput platform for the assessment of ENM-induced hepatotoxicity, which can also be used for pathway analysis and implementation of more conventional biomarker screening. Such an undertaking would best proceed if done in conjunction with animal models to compare the particle-specific effects on participating liver cell types that may be perturbed by ENM exposure.

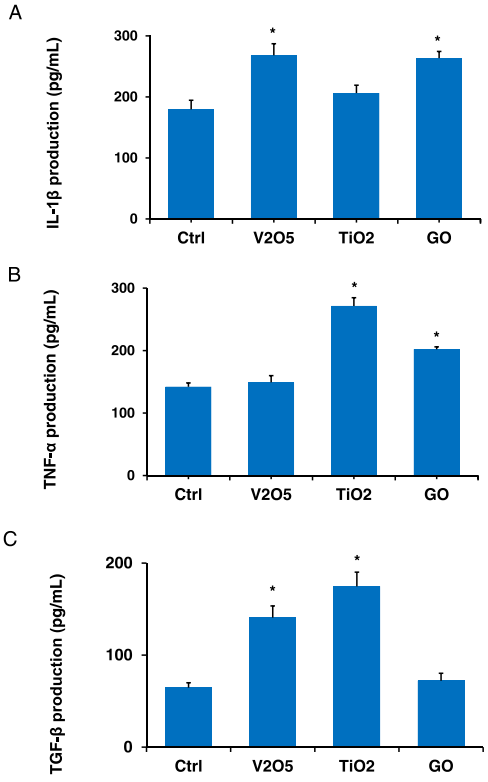

Fig. 8. Determination of NP type-specific cytokine production in 3D liver spheroids. LPS-primed (1 μg/mL, 4 h) liver spheroids were exposed to the NPs for 24 h. Supernatants were collected to measure IL-1β (A), TNF-α (B), and TGF-β1 (C) production by ELISA, respectively. *, p-value < 0.05, shows a significant difference from the control.

Conclusions

In this study, we demonstrate ENMs- and cell-type-specific toxicological responses using scRNAseq technology as well as linked cellular assays in a 3D liver model. The scRNAseq technology allowed us to observe cell-type and NP-specific DEGs and pathways. V_2O_5 NPs were found to exert more adverse effects that involve pro-inflammatory and apoptotic response pathways, as compared to GO and TiO_2. In 3D liver spheroids, NP treatment showed more gene expression alterations and signaling system disruption in hepatocytes than KCs. Importantly, based on findings from scRNAseq, TiO_2 and V_2O_5 NPs were found to cause significant TGF-β production, which has not previously been elucidated. Our studies offer efficient and effective approaches and high-resolution cell-type-specific molecular insights for assessing the impact of nanomaterials on the liver in biomedical applications.

CRediT authorship contribution statement

Jiulong Li: Conceptualization, Methodology, Data curation, Analysis, Writing – original draft. **Graciel Diamante:** Methodology, Investigation, Data curation and Analysis, Visualization, Writing – original draft. **In sook Ahn:** Methodology, Investigation, Data curation, Writing – review & editing. **Darren Wijaya:** Formal analysis, Visualization, Writing – original draft. **Xiang Wang:** Methodology, Data analysis, Validation. **Chong Hyun Chang:** Resources, Investigation, Data curation. **Sung-min Ha:** Data analysis. **Kavya Immadisetty:** Visualization, Writing – original draft. **Huan Meng:** Writing – review & editing. **Andre Nel**: Conceptualization, Funding acquisition, Supervision, Writing – review &editing. **Xia Yang:** Conceptualization, Funding acquisition, Supervision, Writing – review & editing. **Tian Xia:** Conceptualization, Funding acquisition, Supervision, Writing – review & editing.

Data Availability

Data will be made available on request.

Declaration of Competing Interest

Andre E. Nel is a co-founder and equity holder in Westwood Biosciences Inc. and NAMMI Therapeutics. Nel also serves on the Board for Westwood Biosciences Inc. The remaining authors declare no conflicts of interest.

Acknowledgments

The research reported in this publication was supported by the Nanotechnology Health Implications Research (NHIR) Consortium of the National Institute of Environmental Health Sciences of the National Institutes of Health (U01ES027237). The engineered nanomaterials used in the research presented in this publication have been procured/developed, characterized, and provided by the Engineered Nanomaterials Resource and Coordination Core established at Harvard T. H. Chan School of Public Health (NIH grant # U24ES026946). The content is solely the responsibility of the authors and does not necessarily represent the official views of the National Institutes of Health. J. L. was supported by the National Natural Science Foundation of China Youth Program (32201172). GD was supported by an American Diabetes Association Postdoctoral Fellowship (1-19-PDF-007-R).

Appendix A. Supporting information

Supplementary data associated with this article can be found in the online version at doi:10.1016/j.nantod.2022.101652.

References

[1] N. Baig, I. Kammakakam, W. Falath, Nanomaterials: a review of synthesis methods, properties, recent progress, and challenges (http://), Mater. Adv. 2 (2021) 1821–1871, https://doi.org/10.1039/D0MA00807A
[2] B.R. Smith, S.S. Gambhir, Nanomaterials for In Vivo Imaging (http://), Chem. Rev. 117 (2017) 901–986, https://doi.org/10.1021/acs.chemrev.6b00073
[3] E. Valsami-Jones, I. Lynch, How safe are nanomaterials? (http://), Science 350 (2015) 388–389, https://doi.org/10.1126/science.aad0768
[4] Y. Wang, R. Cai, C. Chen, The nano-bio interactions of nanomedicines: understanding the biochemical driving forces and redox reactions (http://), Acc. Chem. Res. 52 (2019) 1507–1518, https://doi.org/10.1021/acs.accounts.9b00126
[5] A. Nel, T. Xia, H. Meng, X. Wang, S. Lin, Z. Ji, H. Zhang, Nanomaterial toxicity testing in the 21st century: use of a predictive toxicological approach and high-throughput screening (http://), Acc. Chem. Res. 46 (2013) 607–621, https://doi.org/10.1021/ar300022h
[6] B. Fadeel, C. Bussy, S. Merino, E. Vázquez, E. Flahaut, F. Mouchet, L. Evariste, L. Gauthier, A.J. Koivisto, U. Vogel, C. Martín, L.G. Delogu, T. Buerki-Thurnherr, P. Wick, D. Beloin-Saint-Pierre, R. Hischier, M. Pelin, F. Candotto Carniel, M. Tretiach, F. Cesca, F. Benfenati, D. Scaini, L. Ballerini, K. Kostarelos, M. Prato, A. Bianco, Safety assessment of graphene-based materials: focus on human health and the environment (http://), ACS Nano 12 (2018) 10582–10620, https://doi.org/10.1021/acsnano.8b04758
[7] X. Lu, Y. Zhu, R. Bai, Z. Wu, W. Qian, L. Yang, R. Cai, H. Yan, T. Li, V. Pandey, Y. Liu, P.E. Lobie, C. Chen, T. Zhu, Long-term pulmonary exposure to multi-walled carbon nanotubes promotes breast cancer metastatic cascades (http://), Nat. Nanotechnol. 14 (2019) 719–727, https://doi.org/10.1038/s41565-019-0472-4
[8] P. Gissen, I.M. Arias, Structural and functional hepatocyte polarity and liver disease (http://), J. Hepatol. 63 (2015) 1023–1037, https://doi.org/10.1016/j.jhep.2015.06.015
[9] Y. Zhang, W. Poon, A.J. Tavares, I.D. McGilvray, W.C.W. Chan, Nanoparticle–liver interactions: cellular uptake and hepatobiliary elimination (http://https://doi.org/), J. Control. Release 240 (2016) 332–348, https://doi.org/10.1016/j.jconrel.2016.01.020
[10] S. Ben-Moshe, S. Itzkovitz, Spatial heterogeneity in the mammalian liver (http://), Nat. Rev. Gastro. Hepat. 16 (2019) 395–410, https://doi.org/10.1038/s41575-019-0134-x

[11] H.F. Teutsch, The modular microarchitecture of human liver (http://https://doi.org/), Hepatology 42 (2005) 317–325, https://doi.org/10.1002/hep.20764

[12] S. Shetty, P.F. Lalor, D.H. Adams, Liver sinusoidal endothelial cells - gatekeepers of hepatic immunity (http://), Nat. Rev. Gastroenterol. Hepatol. 15 (2018) 555–567, https://doi.org/10.1038/s41575-018-0020-y

[13] G. Diamante, I. Cely, Z. Zamora, J. Ding, M. Blencowe, J. Lang, A. Bline, M. Singh, A.J. Lusis, X. Yang, Systems toxicogenomics of prenatal low-dose BPA exposure on liver metabolic pathways, gut microbiota, and metabolic health in mice (http://https://doi.org/), Environ. Int. 146 (2021) 106260, https://doi.org/10.1016/j.envint.2020.106260

[14] F. Heymann, F. Tacke, Immunology in the liver-from homeostasis to disease (http://), Nat. Rev. Gastro. Hepat. 13 (2016) 88–110, https://doi.org/10.1038/nrgastro.2015.200

[15] K. Kazankov, S.M.D. Jørgensen, K.L. Thomsen, H.J. Møller, H. Vilstrup, J. George, D. Schuppan, H. Grønbæk, The role of macrophages in nonalcoholic fatty liver disease and nonalcoholic steatohepatitis (http://), Nat. Rev. Gastro. Hepat. 16 (2019) 145–159, https://doi.org/10.1038/s41575-018-0082-x

[16] M. Bilzer, F. Roggel, A.L. Gerbes, Role of Kupffer cells in host defense and liver disease (http://https://doi.org/), Liver Int. 26 (2006) 1175–1186, https://doi.org/10.1111/j.1478-3231.2006.01342.x

[17] D.A. Hume, The mononuclear phagocyte system (http://https://doi.org/), Curr. Opin. Immunol. 18 (2006) 49–53, https://doi.org/10.1016/j.coi.2005.11.008

[18] A. Boey, H.K. Ho, All roads lead to the liver: metal nanoparticles and their implications for liver health (http://https://doi.org/), Small 16 (2020) 2000153, https://doi.org/10.1002/smll.202000153

[19] V. Mirshafiee, B. Sun, C.H. Chang, Y. Liao, W. Jiang, J. Jiang, X. Liu, X. Wang, T. Xia, A.E. Nel, Toxicological profiling of metal oxide nanoparticles in liver context reveals pyroptosis in kupffer cells and macrophages versus apoptosis in hepatocytes (http://), ACS Nano 12 (2018) 3836–3852, https://doi.org/10.1021/acsnano.8b01086

[20] J. Li, L.M. Guiney, J.R. Downing, X. Wang, C.H. Chang, J. Jiang, Q. Liu, X. Liu, K. Mei, Y. Liao, T. Ma, H. Meng, M.C. Hersam, A.E. Nel, T. Xia, Dissolution of 2D molybdenum disulfide generates differential toxicity among liver cell types compared to non-toxic 2D boron nitride effects (http://https://doi.org/), Small 17 (2021) 2101084, https://doi.org/10.1002/smll.202101084

[21] C. Muoth, A. Wichser, M. Monopoli, M. Correia, N. Ehrlich, K. Loeschner, A. Gallud, M. Kucki, L. Diener, P. Manser, W. Jochum, P. Wick, T. Buerki-Thurnherr, A 3D co-culture microtissue model of the human placenta for nanotoxicity assessment (http://), Nanoscale 8 (2016) 17322–17332, https://doi.org/10.1039/C6NR06749B

[22] M. Štampar, J. Tomc, M. Filipič, B. Žegura, Development of in vitro 3D cell model from hepatocellular carcinoma (HepG2) cell line and its application for genotoxicity testing (http://), Arch. Toxicol. 93 (2019) 3321–3333, https://doi.org/10.1007/s00204-019-02576-6

[23] Y. Ren, R. Geng, Q. Lu, X. Tan, R. Rao, H. Zhou, X. Yang, W. Liu, Involvement of TGF-β and ROS in G1 cell cycle arrest induced by titanium dioxide nanoparticles under UVA irradiation in a 3D spheroid model (http://), Int. J. Nanomed. 15 (2020) 1997–2010, https://doi.org/10.2147/IJN.S238145

[24] S.R. Khetani, S.N. Bhatia, Microscale culture of human liver cells for drug development (http://), Nat. Biotechnol. 26 (2008) 120–126, https://doi.org/10.1038/nbt1361

[25] A. Kermanizadeh, T. Berthing, E. Guzniczak, M. Wheeldon, G. Whyte, U. Vogel, W. Moritz, V. Stone, Assessment of nanomaterial-induced hepatotoxicity using a 3D human primary multi-cellular microtissue exposed repeatedly over 21 days - the suitability of the in vitro system as an in vivo surrogate (http://), Part. Fibre Toxicol. 16 (2019) 42, https://doi.org/10.1186/s12989-019-0326-0

[26] S.V. Llewellyn, M. Niemeijer, P. Nymark, M.J. Moné, B. van de Water, G.E. Conway, G.J.S. Jenkins, S.H. Doak, In vitro three-dimensional liver models for nanomaterial DNA damage assessment (http://https://doi.org/), Small 17 (2021) 2006055, https://doi.org/10.1002/smll.202006055

[27] L. Santos, D. Arneson, K. Chella Krishnan, I.S. Ahn, G. Diamante, I. Cely, A. Butte, A. Lusis, X. Yang, P. Rajbhandari, ScRNA-seq reveals a role of mammary luminal epithelium in adipocyte adaptations (http://), J. Endocr. Soc. 5 (2021) A55, https://doi.org/10.1210/jendso/bvab048.111

[28] T. Tammela, J. Sage, Investigating tumor heterogeneity in mouse models (http://), Annu. Rev. Cancer Biol. 4 (2020) 99–119, https://doi.org/10.1146/annurev-cancerbio-030419-033413

[29] B. Hwang, J.H. Lee, D. Bang, Single-cell RNA sequencing technologies and bioinformatics pipelines (http://), Exp. Mol. Med. 50 (2018) 1–14, https://doi.org/10.1038/s12276-018-0071-8

[30] E. Pennisi, Chronicling embryos, cell by cell, gene by gene (http://), Science 360 (2018) 367, https://doi.org/10.1126/science.360.6387.367

[31] A. Saliba, A.J. Westermann, S.A. Gorski, J. Vogel, Single-cell RNA-seq: advances and future challenges (http://), Nucleic Acids Res. 42 (2014) 8845–8860, https://doi.org/10.1093/nar/gku555

[32] X. Liu, J. Zeng, H. Yang, K. Zhou, D. Pan, V2O5-Based nanomaterials: synthesis and their applications (http://), RSC Adv. 8 (2018) 4014–4031, https://doi.org/10.1039/C7RA12523B

[33] F. Natalio, R. André, A.F. Hartog, B. Stoll, K.P. Jochum, R. Wever, W. Tremel, Vanadium pentoxide nanoparticles mimic vanadium haloperoxidases and thwart biofilm formation (http://), Nat. Nanotechnol. 7 (2012) 530–535, https://doi.org/10.1038/nnano.2012.91

[34] D. Ziental, B. Czarczynska-Goslinska, D.T. Mlynarczyk, A. Glowacka-Sobotta, B. Stanisz, T. Goslinski, L. Sobotta, Titanium dioxide nanoparticles: prospects and applications in medicine (http://), Nanomaterials 10 (2020) 387, https://doi.org/10.3390/nano10020387

[35] B. Dréno, A. Alexis, B. Chuberre, M. Marinovich, Safety of titanium dioxide nanoparticles in cosmetics (http://https://doi.org/), J. Eur. Acad. Dermatol. 33 (2019) 34–46, https://doi.org/10.1111/jdv.15943

[36] V. Georgakilas, J.N. Tiwari, K.C. Kemp, J.A. Perman, A.B. Bourlinos, K.S. Kim, R. Zboril, Noncovalent functionalization of graphene and graphene oxide for energy materials, biosensing, catalytic, and biomedical applications (http://), Chem. Rev. 116 (2016) 5464–5519, https://doi.org/10.1021/acs.chemrev.5b00620

[37] X. Wang, C.H. Chang, J. Jiang, X. Liu, J. Li, Q. Liu, Y. Liao, L. Li, A.E. Nel, T. Xia, Mechanistic differences in cell death responses to metal-based engineered nanomaterials in kupffer cells and hepatocytes (http://https://doi.org/), Small 16 (2020) 2000528, https://doi.org/10.1002/smll.202000528

[38] J. Li, X. Wang, K. Mei, C.H. Chang, J. Jiang, X. Liu, Q. Liu, L.M. Guiney, M.C. Hersam, Y. Liao, H. Meng, T. Xia, Lateral size of graphene oxide determines differential cellular uptake and cell death pathways in Kupffer cells, LSECs, and hepatocytes (http://https://doi.org/), Nano Today 37 (2021) 101061, https://doi.org/10.1016/j.nantod.2020.101061

[39] T. Stuart, A. Butler, P. Hoffman, C. Hafemeister, E. Papalexi, W.M.I. Mauck, Y. Hao, M. Stoeckius, P. Smibert, R. Satija, Comprehensive Integration of Single-Cell Data (http://), Cell 177 (2019) 1888–1902, https://doi.org/10.1016/j.cell.2019.05.031

[40] K.B. Halpern, R. Shenhav, O. Matcovitch-Natan, B. Tóth, D. Lemze, M. Golan, E.E. Massasa, S. Baydatch, S. Landen, A.E. Moor, A. Brandis, A. Giladi, A. Stokar-Avihail, E. David, I. Amit, S. Itzkovitz, Single-cell spatial reconstruction reveals global division of labour in the mammalian liver (http://), Nature 542 (2017) 352–356, https://doi.org/10.1038/nature21065

[41] Z. Nikoozad, M.T. Ghorbanian, A. Rezaei, Comparison of the liver function and hepatic specific genes expression in cultured mesenchymal stem cells and hepatocytes, Iran. J. Basic Med. Sci. 17 (2014) 27–33.

[42] H.C. Fiegel, J.J.H. Park, M.V. Lioznov, A. Martin, S. Jaeschke-Melli, P.M. Kaufmann, B. Fehse, A.R. Zander, D. Kluth, Characterization of cell types during rat liver development (http://https://doi.org/), Hepatology 37 (2003) 148–154, https://doi.org/10.1053/jhep.2003.50007

[43] X. Han, R. Wang, Y. Zhou, L. Fei, H. Sun, S. Lai, A. Saadatpour, Z. Zhou, H. Chen, F. Ye, D. Huang, Y. Xu, W. Huang, M. Jiang, X. Jiang, J. Mao, Y. Chen, C. Lu, J. Xie, Q. Fang, Y. Wang, R. Yue, T. Li, H. Huang, S.H. Orkin, G. Yuan, M. Chen, G. Guo, Mapping the mouse cell atlas by microwell-Seq (http://), Cell 173 (2018) 1307, https://doi.org/10.1016/j.cell.2018.05.012

[44] L. Fei, H. Chen, L. Ma, W. E, R. Wang, X. Fang, Z. Zhou, H. Sun, J. Wang, M. Jiang, X. Wang, C. Yu, Y. Mei, D. Jia, T. Zhang, X. Han, G. Guo, Systematic identification of cell-fate regulatory programs using a single-cell atlas of mouse development (http://), Nat. Genet. 54 (2022) 1051–1061, https://doi.org/10.1038/s41588-022-01118-8

[45] S.A. MacParland, J.C. Liu, X. Ma, B.T. Innes, A.M. Bartczak, B.K. Gage, J. Manuel, N. Khuu, J. Echeverri, I. Linares, R. Gupta, M.L. Cheng, L.Y. Liu, D. Camat, S.W. Chung, R.K. Seliga, Z. Shao, E. Lee, S. Ogawa, M. Ogawa, M.D. Wilson, J.E. Fish, M. Selzner, A. Ghanekar, D. Grant, P. Greig, G. Sapisochin, N. Selzner, N. Winegarden, O. Adeyi, G. Keller, G.D. Bader, I.D. McGilvray, Single cell RNA sequencing of human liver reveals distinct intrahepatic macrophage populations (http://), Nat. Commun. 9 (2018) 4383, https://doi.org/10.1038/s41467-018-06318-7

[46] W. Hu, C. Peng, M. Lv, X. Li, Y. Zhang, N. Chen, C. Fan, Q. Huang, Protein corona-mediated mitigation of cytotoxicity of graphene oxide (http://), ACS Nano 5 (2011) 3693–3700, https://doi.org/10.1021/nn200021j

[47] F. Martinon, J. Tschopp, Inflammatory caspases, and inflammasomes: master switches of inflammation (http://), Cell Death Differ. 14 (2007) 10–22, https://doi.org/10.1038/sj.cdd.4402038

[48] J. Li, C. Chen, T. Xia, Understanding nanomaterial–liver interactions to facilitate the development of safer nanoapplications (http://), Adv. Mater. (2022) 2106456, https://doi.org/10.1002/adma.202106456

[49] P. Godoy, N.J. Hewitt, U. Albrecht, M.E. Andersen, N. Ansari, S. Bhattacharya, J.G. Bode, J. Bolleyn, C. Borner, J. Böttger, A. Braeuning, R.A. Budinsky, B. Burkhardt, N.R. Cameron, G. Camussi, C. Cho, Y. Choi, J. Craig Rowlands, U. Dahmen, G. Damm, O. Dirsch, M.T. Donato, J. Dong, S. Dooley, D. Drasdo, R. Eakins, K.S. Ferreira, V. Fonsato, J. Fraczek, R. Gebhardt, A. Gibson, M. Glanemann, C.E.P. Goldring, M.J. Gómez-Lechón, G.M.M. Groothuis, L. Gustavsson, C. Guyot, D. Hallifax, S. Hammad, A. Hayward, D. Häussinger, C. Hellerbrand, P. Hewitt, S. Hoehme, H. Holzhütter, J.B. Houston, J. Hrach, K. Ito, H. Jaeschke, V. Keitel, J.M. Kelm, B. Kevin Park, C. Kordes, G.A. Kullak-Ublick, E.L. LeCluyse, P. Lu, J. Luebke-Wheeler, A. Lutz, D.J. Maltman, M. Matz-Soja, P. McMullen, I. Merfort, S. Messner, C. Meyer, J. Mwinyi, D.J. Naisbitt, A.K. Nussler, P. Olinga, F. Pampaloni, J. Pi, L. Pluta, S.A. Przyborski, A. Ramachandran, V. Rogiers, C. Rowe, C. Schelcher, K. Schmich, M. Schwarz, B. Singh, E.H.K. Stelzer, B. Stieger, R. Stöber, Y. Sugiyama, C. Tetta, W.E. Thasler, T. Vanhaecke, M. Vinken, T.S. Weiss, A. Widera, C.G. Woods, J.J. Xu, K.M. Yarborough, J.G. Hengstler, Recent advances in 2D and 3D in vitro systems using primary hepatocytes, alternative hepatocyte sources and non-parenchymal liver cells and their use in investigating mechanisms of hepatotoxicity, cell signaling and ADME (http://), Arch. Toxicol. 87 (2013) 1315–1530, https://doi.org/10.1007/s00204-013-1078-5

[50] M.K.R. Donovan, A.D. Antonio-Chronowska, M.D. Antonio, K.A. Frazer, Cellular deconvolution of GTEx tissues powers discovery of disease and cell-type associated regulatory variants (http://), Nat. Commun. 11 (2020) 955, https://doi.org/10.1038/s41467-020-14561-0

[51] A.N. Shami, X. Zheng, S.K. Munyoki, Q. Ma, G.L. Manske, C.D. Green, M. Sukhwani, K.E. Orwig, J.Z. Li, S.S. Hammoud, Single-cell RNA sequencing of human, macaque, and mouse testes uncovers conserved and divergent features of

mammalian spermatogenesis (http://), Dev. Cell 54 (2020) 529–547, https://doi.org/10.1016/j.devcel.2020.05.010
[52] M.A. Heinrich, R. Alert, J.M. LaChance, T.J. Zajdel, A. Košmrlj, D.J. Cohen, J. Rosenblatt, D.Y. Stainier, A. Kabla, Size-dependent patterns of cell proliferation and migration in freely-expanding epithelia (http://), eLife 9 (2020) e58945, https://doi.org/10.7554/eLife.58945
[53] R.D. Hodge, T.E. Bakken, J.A. Miller, K.A. Smith, E.R. Barkan, L.T. Graybuck, J.L. Close, B. Long, N. Johansen, O. Penn, Z. Yao, J. Eggermont, T. Höllt, B.P. Levi, S.I. Shehata, B. Aevermann, A. Beller, D. Bertagnolli, K. Brouner, T. Casper, C. Cobbs, R. Dalley, N. Dee, S. Ding, R.G. Ellenbogen, O. Fong, E. Garren, J. Goldy, R.P. Gwinn, D. Hirschstein, C.D. Keene, M. Keshk, A.L. Ko, K. Lathia, A. Mahfouz, Z. Maltzer, M. McGraw, T.N. Nguyen, J. Nyhus, J.G. Ojemann, A. Oldre, S. Parry, S. Reynolds, C. Rimorin, N.V. Shapovalova, S. Somasundaram, A. Szafer, E.R. Thomsen, M. Tieu, G. Quon, R.H. Scheuermann, R. Yuste, S.M. Sunkin, B. Lelieveldt, D. Feng, L. Ng, A. Bernard, M. Hawrylycz, J.W. Phillips, B. Tasic, H. Zeng, A.R. Jones, C. Koch, E.S. Lein, Conserved cell types with divergent features in human versus mouse cortex (http://), Nature 573 (2019) 61–68, https://doi.org/10.1038/s41586-019-1506-7
[54] A. Butler, P. Hoffman, P. Smibert, E. Papalexi, R. Satija, Integrating single-cell transcriptomic data across different conditions, technologies, and species (http://), Nat. Biotechnol. 36 (2018) 411–420, https://doi.org/10.1038/nbt.4096
[55] P.A. Knolle, G. Gerken, Local control of the immune response in the liver (http://https://doi.org/), Immunol. Rev. 174 (2000) 21–34, https://doi.org/10.1034/j.1600-0528.2002.017408.x
[56] B. Rocque, A. Barbetta, P. Singh, C. Goldbeck, D.G. Helou, Y.E. Loh, N. Ung, J. Lee, O. Akbari, J. Emamaullee, Creation of a single cell RNASeq Meta-Atlas to define human liver immune homeostasis, Front. Immunol. 12 (2021) 2788.
[57] D.E. McCoy, T. Feo, T.A. Harvey, R.O. Prum, Structural absorption by barbule microstructures of super black bird of paradise feathers (http://), Nat. Commun. 9 (2018) 1, https://doi.org/10.1038/s41467-017-02088-w
[58] S.A. MacParland, J.C. Liu, X. Ma, B.T. Innes, A.M. Bartczak, B.K. Gage, J. Manuel, N. Khuu, J. Echeverri, I. Linares, R. Gupta, M.L. Cheng, L.Y. Liu, D. Camat, S.W. Chung, R.K. Seliga, Z. Shao, E. Lee, S. Ogawa, M. Ogawa, M.D. Wilson, J.E. Fish, M. Selzner, A. Ghanekar, D. Grant, P. Greig, G. Sapisochin, N. Selzner, N. Winegarden, O. Adeyi, G. Keller, G.D. Bader, I.D. McGilvray, Single-cell RNA sequencing of human liver reveals distinct intrahepatic macrophage populations (http://), Nat. Commun. 9 (2018) 4383, https://doi.org/10.1038/s41467-018-06318-7
[59] A. Saviano, N.C. Henderson, T.F. Baumert, Single-cell genomics and spatial transcriptomics: discovery of novel cell states and cellular interactions in liver physiology and disease biology (http://), J. Hepatol. 73 (2020) 1219–1230, https://doi.org/10.1016/j.jhep.2020.06.004
[60] S. Akira, K. Takeda, Toll-like receptor signaling (http://), Nat. Rev. Immunol. 4 (2004) 499–511, https://doi.org/10.1038/nri1391
[61] G. Chen, H. Yang, C. Lu, Y. Chao, S. Hwang, C. Chen, K. Lo, L. Sung, W. Luo, H. Tuan, Y. Hu, Simultaneous induction of autophagy and toll-like receptor signaling pathways by graphene oxide, Biomaterials 33 (2012) 6559–6569, https://doi.org/10.1016/j.biomaterials.2012.05.064
[62] V. Kesar, J.A. Odin, Toll-like receptors and liver disease (http://https://doi.org/), Liver Int. 34 (2014) 184–196, https://doi.org/10.1111/liv.12315
[63] G. Szabo, J. Petrasek, Inflammasome activation and function in liver disease (http://), Nat. Rev. Gastro. Hepat. 12 (2015) 387–400, https://doi.org/10.1038/nrgastro.2015.94
[64] K.K. Kim, D. Sheppard, H.A. Chapman, TGF-β1 signaling and tissue fibrosis (http://), Csh. Perspect. Biol. 10 (2018) a22293, https://doi.org/10.1101/cshperspect.a022293
[65] M.I. Setyawati, C. Sevencan, B.H. Bay, J. Xie, Y. Zhang, P. Demokritou, D.T. Leong, Nano-TiO_2 drives epithelial-mesenchymal transition in intestinal epithelial cancer cells (http://https://doi.org/), Small 14 (2018) 1800922, https://doi.org/10.1002/smll.201800922
[66] Y. Zhou, J. Ji, L. Ji, L. Wang, F. Hong, Respiratory exposure to nano-TiO2 induces pulmonary toxicity in mice involving reactive free radical-activated TGF-β/Smad/p38MAPK/Wnt pathways, J. Biomed. Mater. Res. A 107 (2019) 2567–2575, https://doi.org/10.1002/jbm.a.36762
[67] Y. Yu, J. Duan, Y. Li, Y. Li, L. Jing, M. Yang, J. Wang, Z. Sun, Silica nanoparticles induce liver fibrosis via TGF-β(1)/Smad3 pathway in ICR mice, Int. J. Nanomed. 12 (2017) 6045–6057, https://doi.org/10.2147/IJN.S132304 ⟨http://⟩.